

UiO • **Faculty of Mathematics and Natural Sciences**
University of Oslo

Software Beamforming in Medical Ultrasound Imaging

Version 0.2

Ole Marius Hoel Rindal

2022



Preface

This compendium is a rewritten version of the background chapter of my PhD thesis titled “Software Beamforming in Medical Ultrasound Imaging - a blessing and a curse”, defended in November 2019 at the University of Oslo. To bridge a few gaps, some text has also been taken from my MSc thesis from 2014.

Medical ultrasound (US) imaging is a non-invasive imaging modality. Smaller and cheaper US systems make US imaging available to more people, leading to a democratization of medical US imaging. The improvements of general processing hardware allow the reconstruction of US images to be done in software. These implementations are known as software beamforming and provide access to the US data earlier in the processing chain. The UltraSound ToolBox (USTB <https://www.USTB.no>) is an open source processing framework facilitating the comparison of imaging techniques and the dissemination of research results.

Helene Wold and Erlend Akre deserves credit for wrestling LaTeX and changing the format of this text from the original PhD to the official UiO compendium template. Thank you.

Andreas Austeng probably deserves even more credit for withstanding me and being my supervisor for both my master thesis and PhD. Sverre Holm also offered great guidance and supervision. Lastly, my cooperation with Alfonso Rodriques-Molares was very fruitful and resulted in most of the results presented in my PhD dissertation. Alfonso also deserves credit for doing most of the hard work developing the USTB and I benefitted greatly from our cooperation in so many ways ranging from scientific writing to coding.

Contents

Preface	i
Contents	iii
List of Figures	v
1 Scientific Background: Software Beamforming Methodology	1
1.1 A brief history of medical ultrasound imaging	1
1.2 A brief Introduction to beamforming	3
1.3 The physics behind an ultrasound image	7
1.4 The ultrasound probe	9
1.5 Transmission of ultrasound waves	12
1.6 Representing the channel data	15
1.7 Software Beamforming	19
1.8 Adaptive beamforming	34
1.9 Post processing	39
1.10 Speckle statistics	40
1.11 Evaluation of image quality – metrics	43
Appendices	49
A The Hilbert Transform	51
A.1 Analytic signal	51
A.2 Envelope of signal	52
B Deriving the two-way resolution	53
Bibliography	57

List of Figures

1.1	The Siemens Vidoson, press image from Siemens AG, all rights reserved © www.siemens.com/press	2
1.2	Delay and sum beamforming. Figure from (Johnson and Dudgeon, 1993, p. 119)	3
1.3	Source placed at 30 mm, 73.8 mm, 295.2 mm and 500 mm for a array with aperture $D = 12.31$ mm. The first source is very near field, while the second is at the softest far field near field limit $R_1 = \frac{D^2}{4\lambda}$, the third at the strictest $R_2 = \frac{D^2}{\lambda}$ and the fourth is far into far field.	5
1.4	In far field, left, all element have the same direction of propagation ξ , while in near field, right, the ξ_m varies between the elements. (Johnson and Dudgeon, 1993, p.115)	6
1.5	“Focusing in reception. (...) For a particular receive focus position, the signal from all elements can be made to arrive at the same time at a summing amplifier by having an appropriate electronic delay in each channel.” (Whittingham, 2007)	6
1.6	The Philips L7-4 linear array probe imaged in (a) with the geometry and corresponding beampatterns calculated from (1.6) in (b). The vertical lines indicates the -6dB resolution (FWHM) calculated from the approximation formulas in (1.9) and (1.10) and estimated from the beampattern. The x-axis in the plot of the beampatterns is expressed as the lateral axis in the image, relating the angular resolution to the x-axis through a small angle approximation.	10
1.7	The Verasonics P4-2 phased array probe imaged in (a) with the geometry and corresponding beampatterns calculated with (1.6) in (b). The vertical lines indicates the -6dB resolution (FWHM) calculated from the approximation formulas in (1.9) and (1.10) and estimated from the beampattern. The x-axis in the plot of the beampatterns is expressed as the lateral axis in the image, relating the angular resolution to the x-axis through a small angle approximation.	11

List of Figures

1.8	Illustration of three single plane wave images with the top plot showing the transmit waveform delay and the bottom showing the resulting images after beamforming. Note how the steered plane waves (a) and (c) are only illuminating a part of the image, while the plane wave transmitted straight forward (b) is illuminating the entire image. Data from (Liebgott et al., 2016).	13
1.9	Two single transmit images, bottom, created from a DW transmitted at two different transmit angles reconstructed in a sector scan. The transmit waveform delay is plotted in the top. The DW in (a) had a virtual source at $x = 4.8\text{mm}$, $z = -8.3\text{mm}$ and the DW in (b) had a virtual source at $x = -4.8\text{mm}$, $z = -8.3\text{mm}$	14
1.10	Three single transmit images resulting from a single element transmit, as used in STAI imaging. The top plot indicates the firing element, the bottom image is the resulting image. Data from (Rindal, Austeng et al., 2019).	14
1.11	Three single transmit images from a FI transmission in the bottom, with the transmit waveform delay in the top. Data from (Rindal, Rodriguez-Molares and Austeng, 2018)	15
1.12	Part of a RF signal from a single element in the received data used to reconstruct the image in Figure 1.11. The averaged Fourier power spectrum of the full received dataset.	16
1.13	The real, imaginary and the envelope of the analytical signal from a single element in the received data used to reconstruct the image in Figure 1.11. The averaged Fourier power spectrum of the full received analytical dataset in (b). Notice that the analytical signal is a one-sided complex signal.	17
1.14	The real, imaginary and the envelope of the IQ signal from a single element in the received data used to reconstruct the image in Figure 1.11. The averaged Fourier power spectrum of the full IQ dataset in (b). Notice that the spectrum of the IQ signal is complex and centered around 0 MHz.	18
1.15	The envelope detected from the analytical signal (from Figure 1.13a) and the IQ signal (from Figure 1.14a). Notice that the signal are equal, but that the IQ signal should have used a better interpolator than a linear one.	19
1.16	Geometrical illustration of the posed scenario. Figure from (Rindal, Austeng et al., 2019). Credits to Alfonso Rodriguez-Molares for creating the figure.	20
1.17	Receive delay for three different elements (a) the first element, (b) the 64th element and (c) the 128th element.	21
1.18	PW transmit delay for the full image scan for (a) a PW transmitted at -30° , (b) a PW transmitted at 0° , and (c) a PW transmitted at 30°	22
1.19	DW transmit delay for virtual source at (a) $x_s = 4.8, z_s = -8.3\text{ mm}$, (b) $x_s = 0, z_s = -9.6\text{mm}$ and (c) $x_s = -4.8, z_s = -8.3\text{mm}$	22

List of Figures

1.20	Delay geometry for a spherical virtual source as depicted in (Nikolov, Kortbek and J. A. Jensen, 2010). The blue and red indicate the insonified region from two individual transmits. Notice how they overlap in front of, and after the focal point at F . Figure credits to Andreas Austeng creating this figure from (Rindal, Rodriguez-Molares and Austeng, 2018).	23
1.21	Delay geometry for the unified transmit delay model as described in (Nguyen and Prager, 2016). The wavefield is divided into four regions I, II, III and IV. Region I and III follows the spherical model, while the delay for a point \vec{p} in region II and IV is an interpolated value of the delay values in point A and point B. Figure credits to Andreas Austeng creating this figure for (Rindal, Rodriguez-Molares and Austeng, 2018).	24
1.22	Transmit delays for a FI transmission from the center of the array using the (a) spherical, (b) the unified and (c) the hybrid transmit delay model. Figures from (Rindal, Rodriguez-Molares and Austeng, 2018).	25
1.23	Receive apodization for the center pixel $x \approx 0$ mm for the L7-4 probe with depth when using $f\# = 1$. A uniform window is used in (a), while a Hamming window is used in (b).	27
1.24	Conventional scan-line beamforming as implemented in the USTB software beamforming using apodization to make one beam from each transmit.	29
1.25	MLA beamforming with no overlap between the beams. Using 4 MLAs per beam with the transmit masking apodization in the left images, and the resulting single transmit images with the masking applied to the right.	30
1.26	Transmit delays for a FI transmission from the center of the array using the (a) spherical, (b) the unified and (c) the hybrid transmit delay model.	30
1.27	Final images created with MLAs with no overlap to the left, and with overlap to the right. Notice how the image with no overlap have some striping artifacts.	31
1.28	A full FI single Transmit image in (a) the same image in (b) with a suitable transmit masking apodization.	31
1.29	Three single transmit FI images with suitable transmit masking apodization.	32
1.30	(a) is the resulting image from the coherent compounding of the transmit masked single transmit RTB images. The lower amplitude in the focal region is because this region had the least number of overlaps. To compensate for the difference in amplitude, we apply an apodization based on the single transmit apodization masks. The final image is displayed in Figure (b)	33
1.31	The conventional scan-line image in the top left, followed by an interpolated version of the scan-line image, the MLA image and the RTB image. The plot below is the axial line through the group of scatterers close to the foci.	33

List of Figures

1.32	The conventional scan-line image in the top left, followed by an interpolated version of the scan-line image, the MLA image and the RTB image. The plot below is the axial line through the single scatterer almost 30 mm below the foci.	34
1.33	Two images illustration how changing the dynamic range can result in an image where the apparent contrast, in terms of the hypoechoic cyst, seems to be improved. (a) have 60 dB dynamic range, while (b) have 40 dB dynamic range. Data from (Rindal, Austeng et al., 2019).	41
1.34	A STAI image of well developed speckle simulated in Field II.	41
1.35	Estimated PDF of the real and imaginary part of the analytical signal plotted together with the theoretical normal Gaussian distribution.	42
1.36	The estimated PDF of the envelope together with the theoretical Rayleigh distribution.	42
1.37	Full Width Half Maximum (FWHM) measured from a single point scatterer imaged by a plane wave transmission and reconstructed using the DAS, CF, PCF, GCF, MV, EBMV and F-DMAS beamformer.	45
1.38	Images of two point scatterers separated by 1, 0.5 and 0.4 mm in (a), (b) and (c) respectively. The plot below the B-mode images are the lateral line through the center of the points. The red dashed line is indicating -6dB.	46
1.39	The measured separability, measured as the lowest point between the point scatterers, of two point scatterers separated by 4, 2, 1, 0.5, 0.44 and 0.4 mm in (a). The dashed red line indicate the 6dB separation. In (b) we have thresholded on the 6 dB limit, into separated or not separated.	47
A.1	The top is the Fourier spectrum of a signal consisting of two sinususes with frequency 5 and 10. The signal is real so the first spectrum is two-sided. The middle plot is the spectrum of the analytic signal as defined above, and the bottom plot is the Fourier spectrum of just the real part of the analytic signal. We see that as expected no information is lost in the signal.	52
A.2	The top is displaying the signal, the Hilbert transform of the signal and the envelope of the signal. The bottom shows the signal and the envelope of the signal.	52
B.1	The beampattern, a <i>sinc</i> , for some array with size D for some wavelength λ together with a Gaussian with zero mean and some standard variation σ . In the top we have plotted the beampattern and the Gaussian in linear scale, while we in the bottom have plotted them in dB scale. We have also indicated $1/2$ and $1/\sqrt{2}$ in the linear scale, resulting at $\approx -6\text{dB}$ and $\approx -3\text{dB}$ in the dB scale.	53
B.2	The one-way and two-way beampattern plotted indicating that $W_{\text{two way } 6\text{dB}} = W_{\text{one way } 3\text{dB}}$	55

CHAPTER 1

Scientific Background: Software Beamforming Methodology

1.1 A brief history of medical ultrasound imaging

1.1.1 Prototype systems

According to (Szabo, 2013) “the imaginative leap to” ultrasound imaging came with an ultrasound image of the brain. The image was created by the Austrian psychiatrist and neurologist Dr Karl Dussik in 1942. During the pioneering work done in the 1940s and 1950s most of the systems must be considered research prototypes. Worth mentioning are the systems created by Dr. John J. Wild, who modified radar equipment to produce ultrasound images (Szabo, 2013). As well as the “somascop”, an immersion water tank ultrasound system, created by Douglass Howry and Joseph Holmes (Szabo, 2013). A full immersion into a water tank must have been an interesting experience for, hopefully volunteering, patients.

The pioneering work from Inge Edler and Carl Hellmuth Hertz on echocardiography, done at the Lund University in Sweden, also needs to be credited. Through Hertz’s contacts at Siemens (Munich, Germany) they got hold of a modified Siemens reflectoscope, originally created to do material testing (Siemens Healthineers, 2019). They quickly adapted the reflectoscope and applied it to obtain echoes moving synchronously with the heart. The first ultrasound image of a beating heart credited Edler and Hertz was taken on October 1st, 1953. The further development of medical ultrasound scanners accompanied the developments of microelectronics, primarily the breakthrough of integrated circuits and transistors in the late 1940s and 1950s (Szabo, 2013). The improvements in electronics allowed a shift from prototype systems to commercially available systems.

Commercial systems

The first real-time mechanical commercial scanner, the Vidoson from Siemens shown in Figure 1.1, became available in 1964. This scanner quickly became a standard component of assessing pregnant women (Soni, Arntfield and Kory, 2014). Further improvements of the image quality were perhaps, first and foremost, driven by improvements of the transducer arrays such as the

1. Scientific Background: Software Beamforming Methodology

introduction of a 16-channel phased array, the Thaumascan, developed by Von Ramm and Thurstone from Duke University in 1975.

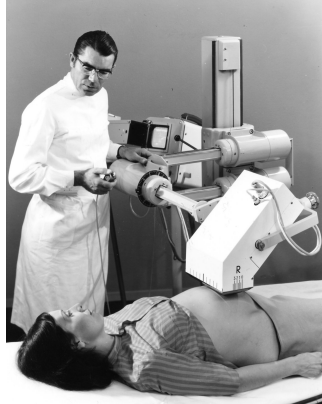


Figure 1.1: The Siemens Vidoson, press image from Siemens AG, all rights reserved © www.siemens.com/press.

Digital systems

Early array systems used analog delay lines to apply the delays to the received signals. However, in the 1990s more powerful microprocessors as well as low-cost analog to digital converters lead the way to replace the complex analog circuitry with digital beamformers. Digital implementations allowed the discovery and development of tissue harmonic imaging which, in some cases, provide superior contrast and detail (Szabo, 2013).

Hand-held systems

The introduction of digital beamformers and general miniaturization of sophisticated electronics paved the way for hand-held systems, now provided by all major ultrasound manufacturers. An exciting development is the introduction of capacitive micromachined ultrasonic transducer (CMUT). CMUT can be printed in silicon together with the electronics to process the signals. The flexibility of CMUT makes a recently established manufacturer (Butterfly Technologies, Guildford, CT, USA) claim that one probe can provide “full body ultrasound”. The images are reconstructed in specialized electronics in the probe, while an iPhone or an Android device is used to display the final images. The ability to do large scale production of CMUT transducers on the same chip as the processing, allows Butterfly to sell their hand-held systems at a very low price. Cheaper and more accessible ultrasound systems are aiding in the democratization of ultrasound imaging (McNeil Jr., 2019).

Software systems

Today, we are at the brink of what can be claimed is another revolution to the ultrasound processing chain: software beamforming. High-end medical ultrasound systems are now utilizing the improvements in the processing power

1.2. A brief Introduction to beamforming

of general hardware and have incorporated software beamforming. To the author's knowledge, only two clinical medical ultrasound vendors utilize software beamforming today; namely the GE Vingmed Ultrasound Vivid systems using the cSound software based beamforming reconstruction platform (Kulina et al., 2016), and the Supersonic Imagine Aixplorer systems (SuperSonic Imagine, 2019). However, extensive publications and many research ultrasound systems are doing software beamforming (Boni et al., 2018) – but only recently has it been brought to the clinic.

1.2 A brief Introduction to beamforming

Beamforming is a variety of array signal processing algorithms that focuses an array's signal capturing abilities in a particular direction (Johnson and Dudgeon, 1993, p. 111-112). In other words, while there are ways to alter the physical antennas to achieve better signal directivity and resolution these physical alterations of an antenna are not reversible nor flexible. Beamforming is to alter the recorded signal data to achieve better directivity and resolution. Beamforming is therefore a cheaper and much more flexible alternative. The drawback of beamforming is increased computation time and more complex signal processing algorithms. The best results are often obtained by a combination of good array properties combined with a sophisticated beamforming technique.

1.2.1 Conventional beamforming

Delay-and-sum (DAS) beamforming is often thought of as the conventional way of doing beamforming. Briefly explained DAS is delaying the signal on each individual sensor to steer in one direction and summing the delayed version of each sensors signal to one output signal. This gives a resulting signal with M (the number of sensors) times better signal to noise ratio than one sensor, e.g. $SNR_{\text{sensor}} = \frac{\sigma_s^2}{\sigma_n^2}$, $SNR_{\text{array}} = M \frac{\sigma_s^2}{\sigma_n^2}$. In other words the array gain is equal to the number of sensors in the array. This simple example assumes uncorrelated white noise. An illustration of DAS beamforming can be seen in Figure 1.2.

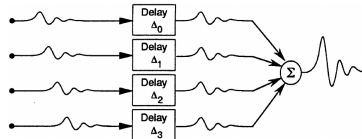


Figure 1.2: Delay and sum beamforming. Figure from (Johnson and Dudgeon, 1993, p. 119).

Mathematically we define the DAS beamformer as

$$z(t) = \sum_{m=0}^{M-1} w_m y_m(t - \Delta_{m,t}) \quad \left| \begin{array}{l} M : \text{Number of elements} \\ m : \text{Element number} \\ w_m : \text{Element weight} \\ y_m : \text{Signal from sensor } m \\ \Delta_{m,t} : \text{Delay for sensor } m \text{ at time } t. \end{array} \right. \quad (1.1)$$

1. Scientific Background: Software Beamforming Methodology

From this definition we see that DAS has another element not yet mentioned; weights. These weights can simply be set to $\frac{1}{M}$, favoring all sensors the same, or we can apply different windows e.g. Hamming which favors the central elements in the array.

Delay-and-sum on vector form

The definition in Equation (1.1) can easily be extended to vector form. We can arrange the different parts of the equation as matrices

$$\mathbf{w} = \begin{bmatrix} w_0 \\ w_1 \\ \vdots \\ w_{M-1} \end{bmatrix}, \widehat{\mathbf{Y}}(t) = \begin{bmatrix} y_0(t) \\ y_1(t) \\ \vdots \\ y_{M-1}(t) \end{bmatrix}, \quad \left| \begin{array}{l} \mathbf{w} : \text{Element weights} \\ \widehat{\mathbf{Y}}(t) : \text{Received signals} \\ \mathbf{Y}(t) : \text{Delayed received signals.} \end{array} \right.$$

$$\mathbf{Y}(t) = \begin{bmatrix} y_0(t - \Delta_0) \\ y_1(t - \Delta_1) \\ \vdots \\ y_{M-1}(t - \Delta_{M-1}) \end{bmatrix}$$

This allows us to simplify Equation (1.1) to

$$z(t) = \sum_{m=0}^{M-1} w_m y_m(t - \Delta_{m,t}) = \mathbf{w}^H \mathbf{Y}(t).$$

Here \mathbf{w}^H is the Hermitian of \mathbf{w} .

We see that the DAS beamformer allows a very simple and fast implementation. It is also very robust, the only assumptions made is that the speed of sound is constant. DAS is therefore one of the most used and best known beamforming techniques.

Near field, far field

When doing array signal processing we need to keep track of the important limit between near field and far field. If the source sending (or reflecting) a signal is in the near field the signal will propagate as a spherical wave. If the transmitting source is further away from the array the signal propagating will locally seem like a plane wave propagating. What actually happens is that the radius of the sphere is so large that the wavefront approaches a plane wave. The limit between far field and near field is defined as (Wright, 1997)

$$R = \frac{D^2}{k\lambda} \quad | \quad k = 1, 2, 3, 4, \dots$$

Since k is an integer we typically choose between 1 and 4, there is no hard limit. The limit depends on how much error we allow, and vary between fields of study.

In Figure 1.3 we have plotted propagating waves from sources placed at different distances from the array. The plots are created with the Field II (J. A. Jensen, 1996)(J. A. Jensen and Svendsen, 1992) simulation environment. It is used an array with 10 elements of width 1 mm placed with pitch $\frac{\lambda}{2}$, giving an

1.2. A brief Introduction to beamforming

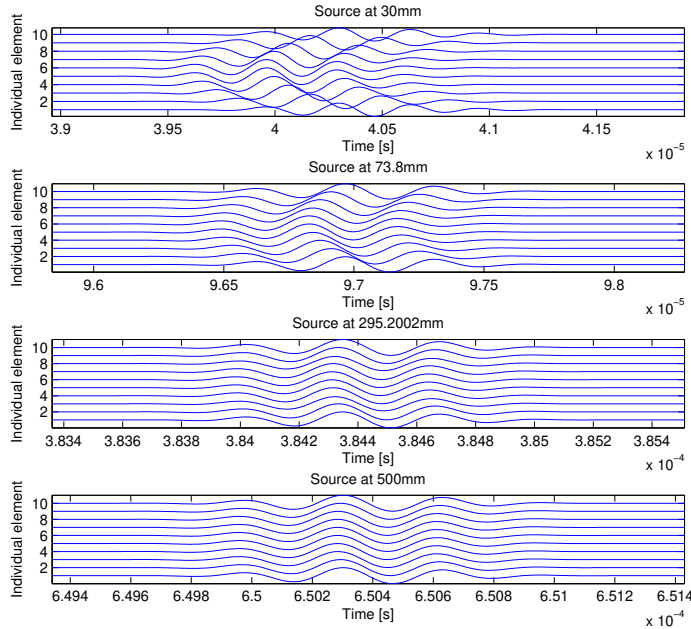


Figure 1.3: Source placed at 30 mm, 73.8 mm, 295.2 mm and 500 mm for a array with aperture $D = 12.31$ mm. The first source is very near field, while the second is at the softest far field near field limit $R_1 = \frac{D^2}{4\lambda}$, the third at the strictest $R_2 = \frac{D^2}{\lambda}$ and the fourth is far into far field.

aperture of $D = 12.31$ mm when the frequency of the signal is 3 MHz assuming speed of sound $c = 1540$ m/s. The softest far field limit is $R_1 = \frac{D^2}{4\lambda} = 73.8$ mm while the strictest is $R_2 = \frac{D^2}{\lambda} = 295.2$ mm. If we look at Figure 1.3 we see that a source placed at R_1 is in the second plot, while a source placed at R_2 in the third plot. From these two plots we clearly see that the wave from R_1 can barely be called plane while the source at R_2 is very close to being plane.

The reason for this digression on far field and near field is because we need to take this into account when finding the delays for the DAS beamformer. For a far field source we can assume that the direction of propagation ξ is equal for all sensors in the array, while for a near field source the direction of propagation varies between the elements in the array, giving a ξ_m for every element. A nice illustration of this can be seen in Figure 1.4. The error we allow between ξ and ξ_m indicates where the far field limit is.

Delay-and-sum in medical ultrasound imaging

The array described in Section 1.2.1 is a typical array used for ultrasound imaging, except that in ultrasound there are typically much more elements. If we for example have 48 elements we get $D \approx 60$ mm giving the softest far field limit $R = \frac{D^2}{4\lambda} = 1757$ mm, so ultrasound is definitely near field. This means that we need to use a technique called dynamic focusing, delaying the

1. Scientific Background: Software Beamforming Methodology

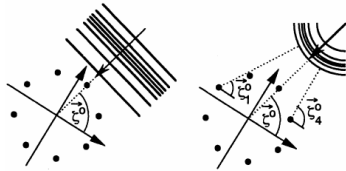


Figure 1.4: In far field, left, all element have the same direction of propagation ξ , while in near field, right, the ξ_m varies between the elements. (Johnson and Dudgeon, 1993, p.115)

signals from the more central elements with respect to those from the outer most elements, this focus is automatically and dynamically advanced to match the depth of origin of echoes (Whittingham, 2007). This will *straighten* the spherical waves recorded before summing them. A nice intuitive illustration of this can be seen in Figure 1.5.

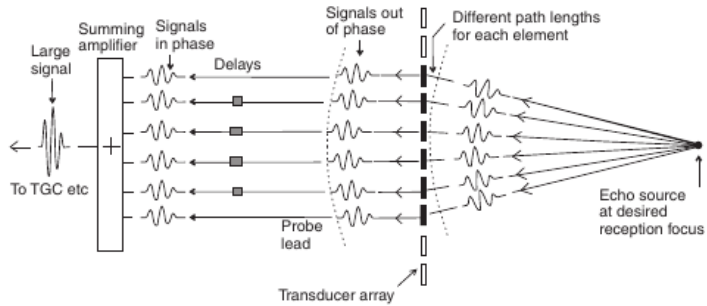


Figure 1.5: “Focusing in reception. (...) For a particular receive focus position, the signal from all elements can be made to arrive at the same time at a summing amplifier by having an appropriate electronic delay in each channel.” (Whittingham, 2007).

1.2.2 Hardware vs. Software Beamforming

Previously, one had to create specialized hardware to do real-time beamforming in an ultrasound system. These hardware implementations typically did one transmit, and processed the received data instantaneously when received. This results in what can be called a "beam based" beamforming approach. Meaning that you are doing your processing per received beam individually. The beamforming approach described in the previous section 1.2 is exactly this type of beambased beamforming. However, for the rest of this compendium we will look into software beamforming and instead of beambased beamforming exploit the flexibility of software beamforming and do what can be known as pixel-based beamforming.

1.2.3 The motivation behind the UltraSound ToolBox

The flexibility of software beamforming provides unprecedented freedom when creating medical ultrasound images. This can be viewed as a *blessing* for

1.3. The physics behind an ultrasound image

the image quality, but a *curse* to the research community. A *curse* since the comparison of methods and research results are becoming more and more challenging with more complex methods published in the literature. The growing number of complex methods makes it hard to make a fair comparison between methods since the re-implementation of a method can be quite challenging. There is no guarantee that the re-implemented method performs as well as the original. To remedy this curse we presented, in (Rodriguez-Molares, Rindal et al., 2017) the UltraSound ToolBox (USTB)¹ which is

“

a processing framework for ultrasound signals. USTB aims to facilitate the comparison of imaging techniques and the dissemination of research results. It fills the void of tools for algorithm sharing and verification, and enables a solid assessment of the correctness and relevance of new approaches. It also aims to boost research productivity by cutting down implementation time and code maintenance. USTB is a MATLAB toolbox for processing 2D and 3D ultrasound data, supporting both MATLAB and C++ implementations. Channel data from any origin, simulated and experimental, and using any kind of sequence, e.g. synthetic transmit aperture imaging (STAI) or coherent plane-wave compounding (CPWC), can be processed with USTB.

”

Most of the work in this thesis was implemented using USTB. The data and implementations to reproduce the results in the publications are presented through [www.USTB.no](http://www.ustb.no). More specifically;

(Rindal, Rodriguez-Molares and Austeng, 2018) at
http://www.ustb.no/publications/paper_II,

(Prieur, Rindal and Austeng, 2018) at
http://www.ustb.no/publications/paper_V,

(Rindal, Rodriguez-Molares and Austeng, 2017) at
http://www.ustb.no/publications/paper_VI,

(Rindal, Austeng et al., 2019) at http://www.ustb.no/publications/paper_VII.

In the current chapter, the medical ultrasound processing chain will be presented, from a software beamforming point of view, as well as pointing to the published work in this thesis where suitable. USTB is used to generate all examples. First, however, we will have a brief look at the physics behind medical ultrasound imaging.

1.3 The physics behind an ultrasound image

Ultrasound waves are longitudinal pressure waves that, by definition, are above the hearable range, meaning higher than ≈ 20 kHz. Medical ultrasound imaging is most often done using frequencies in the range of 2 to 18 MHz. Very shallow imaging, for example, imaging of small animals, is done using higher frequency probes up to ≈ 30 MHz. Higher frequency results in lower penetration depth

¹Alfonso Rodriguez-Molares deserves credits for most of the heavy lifting in the development of USTB.

1. Scientific Background: Software Beamforming Methodology

because of the frequency-dependent attenuation of tissue. The benefit of higher frequency is improved resolution. Thus, ultrasound imaging results in a trade-off between penetration depth and resolution.

The wave equation describes the propagation of a wave. The lossless wave equation is, see e.g. (Holm, 2019)

$$\Delta^2 u - \frac{1}{c^2} \frac{\partial^2 u}{\partial t^2} = \frac{\partial^2 u}{\partial x^2} + \frac{\partial^2 u}{\partial y^2} + \frac{\partial^2 u}{\partial z^2} - \frac{1}{c^2} \frac{\partial^2 u}{\partial t^2} = 0 \quad (1.2)$$

where Δ is the Laplacian operator, c is the speed of sound, x, y, z is the spatial coordinates, t is time, u is the displacement vector. The displacement vector u can also be replaced with the scalar pressure p .

The wave equation comes in many adaptations. One of them is the viscous wave equation which includes a term to model the frequency-dependent attenuation, see e.g. (Holm, 2019)

$$\Delta^2 u - \frac{1}{c^2} \frac{\partial^2 u}{\partial t^2} + \tau c^2 \frac{\partial}{\partial t} \Delta^2 u = 0. \quad (1.3)$$

Here $\tau = \frac{\eta}{E}$, with E being the elastic modulus and η the viscosity. The frequency dependence of the absorption can be derived from the last term. The frequency-dependent absorption results in limitations on which frequency can be used to image deeper parts and organs in the body.

The high-frequency wave transmitted into the body will propagate according to the wave equation as long as the medium has similar acoustic properties. If the properties change, a part of the wave will be reflected, while another part will continue to propagate through the medium. The pressure reflection coefficient is given by

$$R = \frac{Z_1 - Z_2}{Z_1 + Z_2} = \frac{\rho_1 c_1 - \rho_2 c_2}{\rho_1 c_1 + \rho_2 c_2}, \quad (1.4)$$

where Z is the acoustic impedance of the medium, ρ is the medium density, and c is the speed of sound. The transmitted wave's direction is given by the angle θ_t dependent on the angle of incidence angle θ_i . Snell's law gives both angles,

$$\frac{c_1}{c_2} = \frac{\sin \theta_t}{\sin \theta_i}. \quad (1.5)$$

Snell's law describes the reflections happening at distinct boundaries between two media with different acoustic properties. The reflections governed by Snell's law is known as geometrical scattering and results in specular reflections. This is one of three types of scattering. The three types are dependent on the size of the object scattering the sound - the scatterer. When the scatterer is much larger than the wavelength of the transmitted wave, we have geometrical scattering with specular reflections. Rayleigh scattering, also known as diffuse scattering, occurs when the scatterer is much smaller than the transmitted wavelength. If enough small scatterers are present, we get multiple scattering, resulting in the well-known speckle pattern in ultrasound imaging. The statistical distribution of speckle in ultrasound is well known (see Section 1.10). The third type of scattering is when the scattering structure is comparable to the size of the transmitted wavelength.

In summary, some of the signals transmitted into the body will be reflected or scattered back and recorded by the ultrasound probe, which transmitted the signal. In all, only 1 % of the sound waves transmitted into the body return to the probe (Soni, Arntfield and Kory, 2014).

1.4 The ultrasound probe

In medical ultrasound imaging, the waves are transmitted into the body using a probe consisting of an array of elements. A two-dimensional array is used for 3D imaging. We will restrict ourselves to 2D imaging and consider two variants of one-dimensional ultrasound probes: a linear and a phased array. Conventionally the elements of a probe are made from piezoelectric ceramics, exploiting the piezoelectric effect to create the ultrasound signal.

1.4.1 Linear array

We will use the L7-4 (Philips, Amsterdam, NL) probe shown in Figure 1.6 to describe a conventional linear array. The array consists of 128 elements with a pitch, the distance between the center of the elements, of 0.2980 mm. The height of the elements is 7 mm. Using a center frequency of 5.2 MHz results in $\approx \lambda$ pitch, where $\lambda = c/f$ is the wavelength. To characterize the probe we make some assumptions. We assume that the response in focus is similar to the far-field response (Steinberg, 1976), and assume point sources. The beampattern can then be calculated by the discrete aperture smoothing function, the discrete Fourier transform, of an array along the x-axis as, see e.g., (Johnson and Dugdeon, 1993)

$$W(k_x)_{\text{one way}} = \sum_{m=0}^{M-1} w_m e^{j k_x x_m}. \quad (1.6)$$

Here w_m is the element weight, k_x is the x component of the wavenumber vector, and x_m is the element position. The relation between k_x and the incidence angle θ of the wave is, $k_x = -k \sin \theta = -\frac{2\pi}{\lambda} \sin \theta$ (Johnson and Dugdeon, 1993). Using (1.6) and assuming a narrow band with a center frequency of $f_c = 5.2$ MHz we get the beampattern for the L7-4 probe as plotted in the top plot of Figure 1.6b. The x-axis in the plot is expressed as the lateral axis in the image, relating the angular resolution to the x-axis through a small angle approximation. The small angle approximation means it is only valid around the focus center, around the main-lobe, which is what we are mostly interested in.

In ultrasound imaging, we are first transmitting and then receiving the signal. When using a focused transmit and receive, and assuming we use the full array for both, the final response of the probe is given by the two way beampattern, which can be calculated by (Johnson and Dugdeon, 1993)

$$W_{\text{two way}} = W_{tx} W_{rx} = W_{\text{one way}}^2. \quad (1.7)$$

The two way beampattern for the L7-4 probe is plotted in the lower plot of Figure 1.6b. The beampattern is often used to characterize the resolution of a system. There exist many definitions of the resolution but perhaps the most used is the -6 dB width of the mainlobe, also known as the full width half

1. Scientific Background: Software Beamforming Methodology

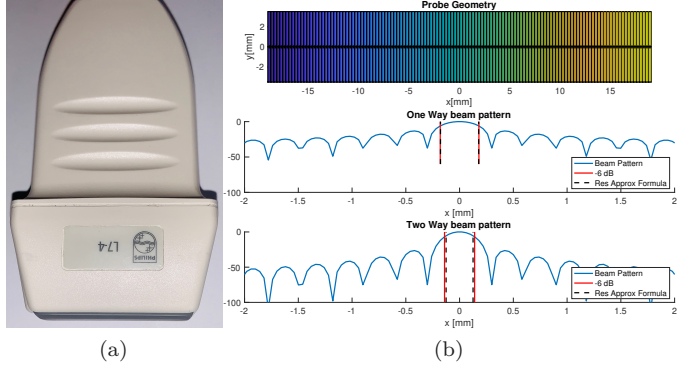


Figure 1.6: The Philips L7-4 linear array probe imaged in (a) with the geometry and corresponding beampatterns calculated from (1.6) in (b). The vertical lines indicates the -6dB resolution (FWHM) calculated from the approximation formulas in (1.9) and (1.10) and estimated from the beampattern. The x-axis in the plot of the beampatterns is expressed as the lateral axis in the image, relating the angular resolution to the x-axis through a small angle approximation.

maximum (FWHM). For a linear array, the angular resolution at -6 dB can be approximated by (Harris, 1978)

$$\theta_{6dB} \approx \frac{1.21\lambda}{D}, \quad (1.8)$$

where D is the size of the full array aperture. Notice how the resolution is inverse proportional to the size of the array, and proportional to the signal frequency through the wavelength λ . The spatial lateral resolution at a certain depth, z , can be found using a small angle approximation

$$x_{res} = z\theta_{6dB} = z \frac{1.21\lambda}{D} = 1.21\lambda f\#. \quad (1.9)$$

Here we defined the f-number $f\# = \frac{z}{D}$ as the ratio between the depth and the size of the aperture D . We will later, in Section 1.7.2 see how we can use receive apodization to reconstruct a constant $f\#$ giving uniform resolution in the final image. For the x-axis in Figure 1.6b we have used this small angle approximation and assumed that $z = D$, thus that the $f\# = 1$.

An approximation for the two-way resolution, see derivation in Appendix A, assuming the same array has been used for both transmit and receive is

$$x_{res \text{ two way}} \approx \frac{1.21\lambda z}{\sqrt{2}D}. \quad (1.10)$$

In Figure 1.6b we have estimated the -6 dB resolution found from the beampattern, and by using the approximation formulas in (1.9) and (1.10). From the figure, we see that the approximation fits pretty good.

1.4.2 Phased array

To demonstrate a typical phased array, we will use the P4-2 probe from Verasonics (Kirkland, Washington, USA) shown in Figure 1.7a. The P4-2

1.4. The ultrasound probe

array has 64 elements with a pitch of 0.3 mm. Assuming a center frequency of 2.9 MHz, we get the beampatterns, using the same assumptions as earlier, calculated with (1.6) in Figure 1.7b.

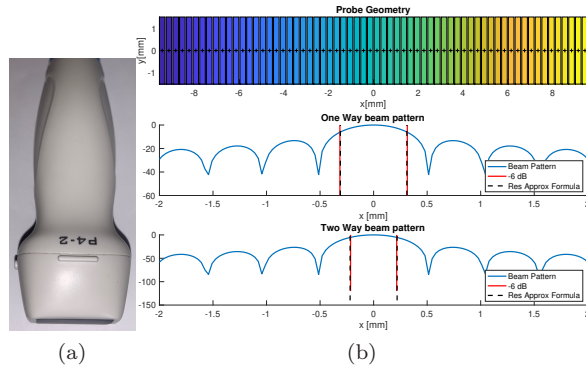


Figure 1.7: The Verasonics P4-2 phased array probe imaged in (a) with the geometry and corresponding beampatterns calculated with (1.6) in (b). The vertical lines indicates the -6dB resolution (FWHM) calculated from the approximation formulas in (1.9) and (1.10) and estimated from the beampattern. The x-axis in the plot of the beampatterns is expressed as the lateral axis in the image, relating the angular resolution to the x-axis through a small angle approximation.

Notice that the resolution of the P4-2 array is significantly lower than for the L7-4 probe. The resolution is lower because of the smaller array and the lower frequency used for cardiology. To be able to image between the ribs, the array must be smaller, and the lower frequency is necessary to penetrate deep enough to image the full heart. The phased array gets its name from the fact that most cardiac applications use transmits beams at steered angles, resulting in a sector scan. While a linear array usually transmits straight forward-focused beams in front of the transducer resulting in a linear scan. However, in Section 1.5, we will see that the flexibility of software beamforming allows many kinds of transmit beams.

1.4.3 Elevation resolution

The resolution in the elevation dimension can be derived using the same analysis as we did for the axial dimension. However, the elevation resolution is dependent on the element height or for a 2D array, the array of elements in the elevation dimension.

1.4.4 Axial resolution

For completeness, we will add that the axial resolution is independent of the probe geometry but dependent on the transmit pulse. A rule of thumb for the axial resolution is (Franceschetti and Lanari, 1999)

$$z_{\text{res}} = \frac{c}{2B}, \quad (1.11)$$

where c is the speed of sound, and B is the transmitted pulse bandwidth.

1.5 Transmission of ultrasound waves

Ultrasound imaging uses the pulse-echo principle. Meaning that the ultrasound wave is transmitted from the probe, and after the wave is transmitted, the same probe starts to receive the ultrasound signal reflected, echoed, from the body. The ultrasound wave travels with the speed of sound, typically assumed to be 1540 m/s for the body. The next wave cannot be transmitted before the two-way travel time from the deepest point in the image to be reconstructed, have been reached. Several, up to hundreds, of transmits are used per image effectively limiting the imaging frame rate. The best image quality is obtained if there is a focused transmit and a focused receive. Conventionally, this was done using a focused transmission, with a dynamic focusing applied on receive through the beamforming process, see Section 1.7. However, a focused transmission is illuminating only a small region of the image, and thus, a large number of transmits are needed resulting in a relatively low frame rate. Modern beamforming techniques utilize variously unfocused transmit waveforms. These unfocused transmit waveforms can synthetically be combined to recreate a focused transmission by a technique known as coherent compounding, see Section 1.7.4. We will now consider the three most typical types of transmit waveforms: planar, diverging, and converging. These three transmit waveforms can be used to create the four most used types of imaging modalities known as plane wave imaging, diverging wave imaging, synthetic transmit aperture imaging, and focused imaging.

1.5.1 Plane Waves (PW)

The breakthrough of coherent plane wave compounding (CPWC) imaging came with the paper published by Montaldo et al., 2009. They showed that very high frame rate imaging is possible by utilizing planar transmits. Higher quality images can be achieved by coherently compounding multiple plane wave images. The high frame rate is possible because a plane wave illuminates a large, or the full, region one wants to image. This greatly reduces the number of transmits necessary to form an image. To illustrate this, we allow ourselves to make a leap forward in our understanding of ultrasound imaging and assume that we know how to recreate an ultrasound image. Thus, in Figure 1.8, three resulting images from single plane wave transmissions are shown. The time each element transmitted the ultrasound pulse, the transmit waveform delay, is plotted. The transmit waveform delay illustrates how we can steer the plane waves at different transmit angles. Notice how the plane waves steered at an angle in Figure 1.8 (a) and (c) only illuminates a part of the image, while the plane wave transmitted straight forward (b) is illuminating the entire image. An individual plane wave image has quite low quality in terms of contrast and resolution. However, for some applications such as Doppler imaging of the blood, the benefits of high frame rate outweigh the low image quality. Higher image quality, comparable to a fully focused image, can be obtained if enough plane waves transmitted at different angles are coherently compounded (Montaldo et al., 2009). However, coherent compounding is sensitive to targets moving between transmits, and the assumption of a plane wave is only valid in a certain region along with the propagating wave. Outside the region, "edge waves" not following a plane propagation degrades the image quality since the plane wave assumption does

1.5. Transmission of ultrasound waves

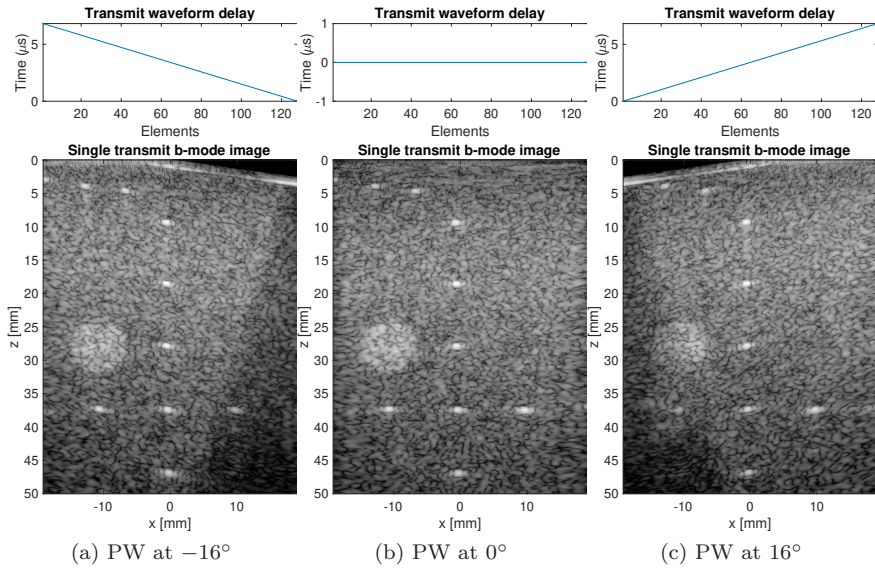


Figure 1.8: Illustration of three single plane wave images with the top plot showing the transmit waveform delay and the bottom showing the resulting images after beamforming. Note how the steered plane waves (a) and (c) are only illuminating a part of the image, while the plane wave transmitted straight forward (b) is illuminating the entire image. Data from (Liebgott et al., 2016).

not hold.

1.5.2 Diverging Waves (DW)

To have an even broader illumination of a region, one can transmit diverging waves. As illustrated in Figure 1.9 these images are illuminating a sector growing with depth, making it suitable for a sector scan used in, for example, cardiac imaging. Cardiac imaging uses a sector scan since it is restricted to a narrow *acoustical window* between the ribs. And thus, diverging waves are mostly applied for cardiac applications as described in (Papadacci et al., 2014). The same discussion on the pros and cons of PWs applies to DWs, where higher image quality can be obtained by coherently compounding multiple low-quality images.

1.5.3 Synthetic Transmit Aperture Imaging (STAI)

The images with the highest image quality are created by synthetic transmit aperture imaging (STAI). With STAI imaging, we mean transmitting on every single consecutive element but receiving on the full array, see for example (J. A. Jensen, Nikolov et al., 2006). STAI has some obvious drawbacks such as penetration depth, and as with DWs and PWs the coherent compounding is sensitive to imaging moving targets. The limited penetration depth has been, slightly, improved by instead of firing a single element firing on a group of elements. In both cases, a diverging wave originating from the center of

1. Scientific Background: Software Beamforming Methodology

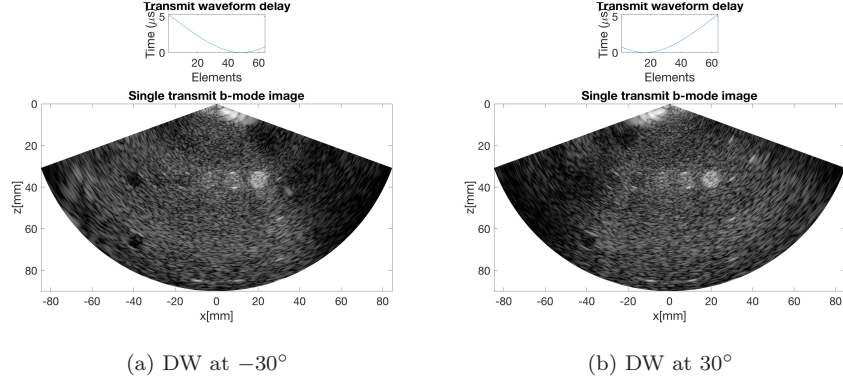


Figure 1.9: Two single transmit images, bottom, created from a DW transmitted at two different transmit angles reconstructed in a sector scan. The transmit waveform delay is plotted in the top. The DW in (a) had a virtual source at $x = 4.8\text{mm}$, $z = -8.3\text{mm}$ and the DW in (b) had a virtual source at $x = -4.8\text{mm}$, $z = -8.3\text{mm}$.

the firing element(s) is formed. The high image quality is obtained because we create a synthetic focus in the reconstruction. Compared to PW and DW imaging, the assumption of a diverging wave from each element holds for the entire propagation of the wave. Figure 1.10 shows three images created from single element transmission; the top plot now indicates the transmitting element.

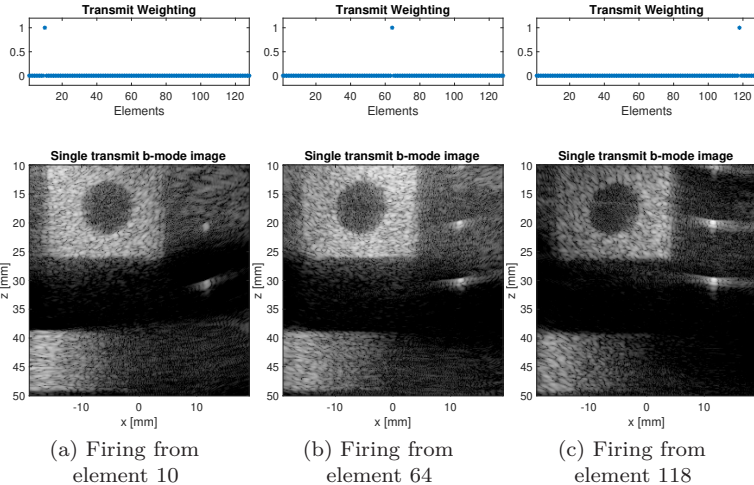


Figure 1.10: Three single transmit images resulting from a single element transmit, as used in STAI imaging. The top plot indicates the firing element, the bottom image is the resulting image. Data from (Rindal, Austeng et al., 2019).

1.5.4 Focused Imaging (FI)

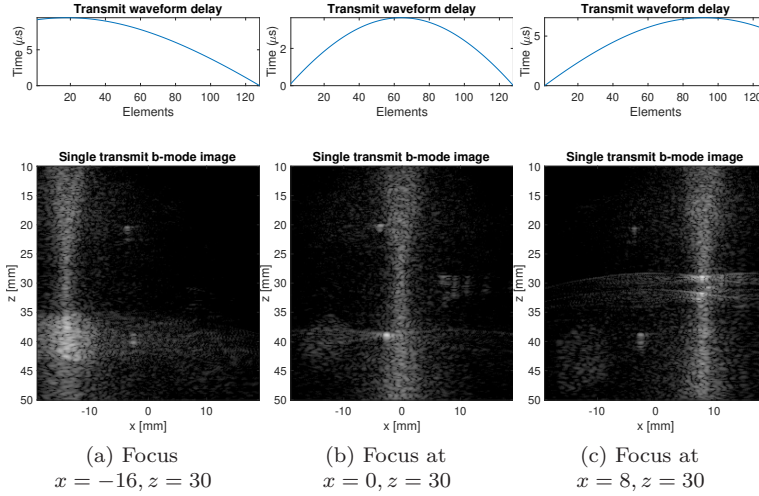


Figure 1.11: Three single transmit images from a FI transmission in the bottom, with the transmit waveform delay in the top. Data from (Rindal, Rodriguez-Molares and Austeng, 2018)

Historically ultrasound transmissions where focused transmission meaning a first converging, towards a focus point, and then diverging wave front. This is still, to the authors knowledge the most used type of transmit in modern ultrasound systems. Conventionally, one transmit results in one *scan-line* in the final image. Typically tens to hundreds of transmits are used per image. With the flexibility of software beamforming we can, as with the previous imaging modalities, recreate the full image from a single transmit. This can be exploited in more sophisticated imaging techniques such as in multi line acquisitions (MLA, see Section 1.7.6) and retrospective beamforming (RTB, see Section 1.7.7). RTB, and to a certain degree MLA, recreates a synthetic focus in the overlapping regions between transmits, generating a synthetic focus through coherent compounding resulting in a fully focused image. To illustrate the waveform resulting from FI imaging, we have reconstructed the full image from single focused transmits in Figure 1.11, with the transmit element waveform delays plotted in the top.

It is worth to mention, without going two deep into non-linear acoustics, that FI images have benefits over PW, DW, and STAI imaging regarding second harmonics imaging. FI obtains higher peak pressure in the body, which generates more non-linearity resulting in more second harmonics generated.

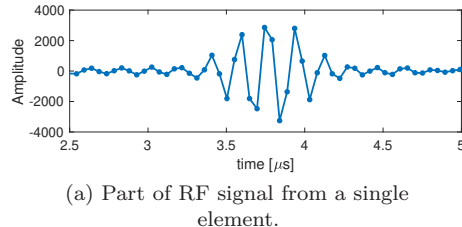
1.6 Representing the channel data

The ultrasound waveforms are transmitted into the body. The reflected signals are recorded with the array of elements in the ultrasound probe. Signals originating from deeper inside the body will be more attenuated than signals from shallow reflections. The signals are time gain compensated (TGC) to

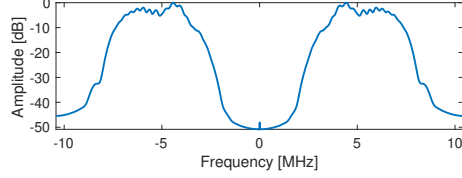
compensate for this attenuation. We will, from now on, assume that all signals have gone through appropriate TGC. Now, we will look at three different ways of representing the received channel data, as RF (radio frequency) data, as the analytical signal or as (In-phase Quadrature) IQ data.

1.6.1 RF-channel data

If we know our signal processing, including the Nyquist sampling criteria, we should sample the data at twice the highest frequency. Theoretically, this should be fine, however practically sampling at a higher frequency makes designing receiving filters easier. We will denote the RF-channel data as the channel data sampled according to the Nyquist sampling criteria.



(a) Part of RF signal from a single element.



(b) Fourier power spectrum of a full data set.

Figure 1.12: Part of a RF signal from a single element in the received data used to reconstruct the image in Figure 1.11. The averaged Fourier power spectrum of the full received dataset.

As an example, we will consider the RF-channel data as generated by the Verasonics Vantage 256 system. Here, the default sampling rate is four times the transmitted center frequency. The channel data used to recreate the FI images in Section 1.5.4 were transmitted using a center frequency $f_c = 5.208$ MHz and sampled with a sampling frequency of $f_s = 4f_c = 20.83$ MHz. In Figure 1.12a, we have plotted a part of the signal received on element 10 for one of the transmits. In Figure 1.12b, we have plotted the averaged Fourier power spectrum of the full data set.

The analytical signal

In medical ultrasound imaging, our result is an image of the received signal envelope. A convenient way of detecting the envelope is to use the analytical signal, which is defined as

$$x_a(n) = x(n) + j(\hat{x}(n)), \quad (1.12)$$

where x is the RF signal, while \hat{x} is the Hilbert transform of x .

1.6. Representing the channel data

The envelope can be detected by simply taking the magnitude of the analytical signal $a(n) = |x_a[n]| = \sqrt{x(n)^2 + \hat{x}(n)^2}$. Figure 1.13a shows the analytical signal from the same FI data set from Section 1.5.4, and Figure 1.13b is its Fourier power spectrum. Notice, from the power spectrum, that the analytical signal is a one-sided complex signal.

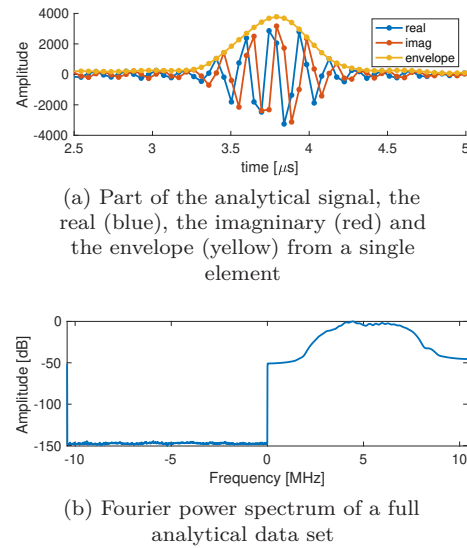


Figure 1.13: The real, imaginary and the envelope of the analytical signal from a single element in the received data used to reconstruct the image in Figure 1.11. The averaged Fourier power spectrum of the full received analytical dataset in (b). Notice that the analytical signal is a one-sided complex signal.

The benefit of using the analytical signal, as we do in the USTB, is that it makes it easier to do envelope detection after beamforming. Using the analytical signal throughout the beamforming relaxes the number of axially reconstructed pixels. It also facilitates some adaptive beamforming techniques, that we will get back to in Section 1.8, such as Capon's minimum variance beamforming. The Capons minimum variance technique needs to create complex weights and needs to be able to create unsymmetric, in frequency space, weight sets. Complex data also facilitates some Doppler-techniques.

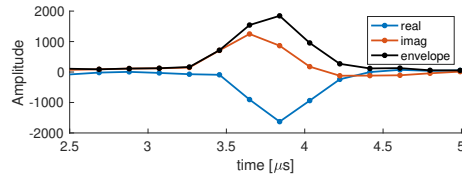
1.6.2 IQ-channel data

The received ultrasound signal is bandlimited. Therefore, one can obtain more compact forms of storing the bandlimited signal through the In-phase Quadrature (IQ) signal. There are multiple definitions and variations of the IQ-signal. We will, however, briefly look into two ways the IQ-signal can be obtained. The first approach is to demodulate the RF signal into the IQ-signal. The second approach is to undersample the signal.

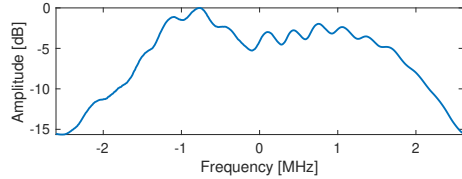
Demodulation

To describe demodulation, let's reuse a slightly modified text from (Palmer et al., 2016)

1. Scientific Background: Software Beamforming Methodology



(a) Part of the IQ signal, the real, the imaginary and the envelope from a single element.



(b) Fourier power spectrum of a full IQ data set.

Figure 1.14: The real, imaginary and the envelope of the IQ signal from a single element in the received data used to reconstruct the image in Figure 1.11. The averaged Fourier power spectrum of the full IQ dataset in (b). Notice that the spectrum of the IQ signal is complex and centered around 0 MHz.

“

The concept of In-phase Quadrature (IQ) data sampling is worth a brief explanation, for a more thorough description, see (Proakis and Manolakis, 2007). When we have a bandlimited RF-signal centered around a center frequency, the IQ-signal can be obtained by down-mixing the signal. Down-mixing means multiplying the signal with a complex sinusoid signal given by a demodulation frequency f_{demod} “moving down” the signal in the frequency spectrum by using a negative demodulation frequency. This gives an asymmetrical and thus complex signal. This signal can then be low-pass filtered removing the frequencies and noise outside the desired bandwidth. This lowpass-filtered signal can then be decimated reducing the number of samples by a integer factor, in our case 4 compared to the default Verasonics RF-sampling frequency. However, we need to keep in mind that the IQ-sample is complex, thus having both a real and an imaginary part.

”

If we take the same signal as earlier and do this demodulation process, we end up with the complex IQ-signal plotted in Figure 1.14a with the frequency spectrum in Figure 1.14b. Notice that the spectrum of the IQ signal is complex and centered around 0 MHz, since a demodulation frequency equal to the center frequency was used.

The benefit of using the IQ signal is that it reduces the number of samples, allows easy detection of the envelope, and that it facilitates beamforming and Doppler-techniques that need complex data. An illustration of the reduction of samples, but not losing information, can be seen by comparing the envelope from the analytical signal with the envelope of the IQ-signal plotted in Figure 1.15. Note that a better interpolator than linear interpolations should have been used.

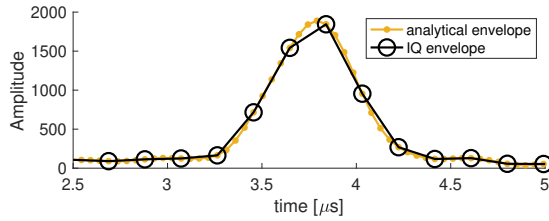


Figure 1.15: The envelope detected from the analytical signal (from Figure 1.13a) and the IQ signal (from Figure 1.14a). Notice that the signals are equal, but that the IQ signal should have used a better interpolator than a linear one.

Bandwidth sampling (Undersampling)

A second way of obtaining a variant of an IQ-signal is to do bandwidth sampling, or undersampling, of the signal directly. An intuitive explanation of this can be found in a whitepaper from Verasonics (Kaczkowski, 2016). Here one sets the Nyquist sampling rate below the transducers frequency response and samples the aliased or a down-folded version of the bandlimited signal. However, to be able to do this, one needs to be able to filter out the "unwanted" signal, which might already be present in the band the desired signal aliases into. Verasonics solves this by having programmable analog low-and highpass filters filtering out the signals before they allow the wanted signal to be folded down.

1.7 Software Beamforming

Beamforming denotes the process of going from the recorded channel data to a combined estimate of the reflection coefficient displayed in the final image. This section will describe the individual steps namely the wave travel time delay calculations (Section 1.7.1), the combination of the delayed signals with the delay and sum algorithm (Section 1.7.2), a closer look at the coherent compounding (Section 1.7.4) as well as going through the differences between scan-line beamforming (Section 1.7.5), multiple line acquisitions (MLA, Section 1.7.6) beamforming, and retrospective beamforming (RTB, Section 1.7.7). We will, for simplicity, only consider a linear scan in the rest of this chapter. Even though modifying the calculations to using polar coordinates facilitates the same techniques for a sector scan. However, let us first introduce beamforming by reusing some notation, definitions, and a figure from (Rindal, Austeng et al., 2019).

Without loss of generality let us assume a linear array of M elements, laying on the x -axis, pointing towards the positive direction of the z -axis, as illustrated in Fig. 1.16. The domain, with characteristic sound speed c_0 , is illuminated by a generic transmit beam, either planar, converging or diverging. Let us denote the signal received by element m as $h_m(t)$. Let us denote as T the distance from the origin of the transmitted wave to the point (x, z) , and as R the distance from (x, z) to the location of element m and as o the offset to compensate for the center of the pulse and time zero convention. If we apply

” ”

“

the propagation delay,

$$\Delta t = (T + R)/c_0 - o, \quad (1.13)$$

we obtain the signal value at (x, z) received by element m ,

$$s_m = h_m(t)|_{t=\Delta t}, \quad (1.14)$$

also referred to as *pixel value*. Note that we drop the spatial coordinates (x, z) . The symbol s_m refers to the pixel value at an arbitrary location (x, z) , unless otherwise specified.

”

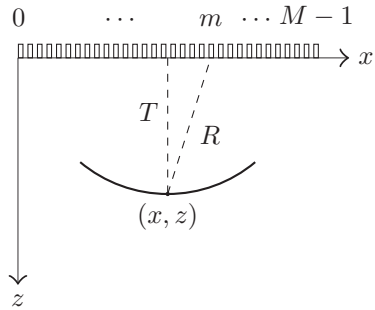


Figure 1.16: Geometrical illustration of the posed scenario. Figure from (Rindal, Austeng et al., 2019). Credits to Alfonso Rodriguez-Molares for creating the figure.

1.7.1 Delay Calculation

Beamforming can be viewed as a geometrical problem. Let us, therefore, have a look at the delay calculations involved in software beamforming. We will calculate the delays assuming *the general beamformer* as used in the USTB (Rodriguez-Molares, Rindal et al., 2017)

“

[...] around the concept of the general beamformer. The wavefronts in most ultrasound sequences can be fully defined using a single point source P : in focused imaging (FI) and retrospective transmit beamforming (RTB) P is on the transmit focal point in front of the probe, in diverging wave imaging (DWI) P is at the wave origin behind the probe, in synthetic transmit aperture imaging (STAII) P lies on the active element, in coherent plane-wave compounding (CPWC) P is at an infinite distance but in a given direction. Using point sources to define all those waves it is possible to beamform all sequences with a single algorithm.

”

To further comply with the general beamformer, we assume that the channel data have been compensated to fulfill the time zero convention used in the USTB. In the USTB we have defined "that time zero corresponds to the moment the transmitted wave passes through the origin of coordinates $(0,0,0)$ " (Rodriguez-Molares, Rindal et al., 2017). We will, for simplicity, restrict ourselves to 2D

1.7. Software Beamforming

imaging and have a closer look at how the receive distance R and the transmit distance T from (1.13) can be calculated.

Receive delay

The receive distance R from (x, z) to the location of element m is independent of the type of transmit and can be calculated as

$$R(x, z, m) = \sqrt{z^2 + (x - m)^2}. \quad (1.15)$$

If we assume that we are imaging with the 128 elements L7-4 probe as defined in Section 1.4.1, and define a linear scan of pixels with 512 pixels from $x = -19$ mm to $x = 19$ mm and 512 pixels from $z = 0$ to $z = 50$ mm the receive delays can be visualized, four three of the elements, as in Figure 1.17.

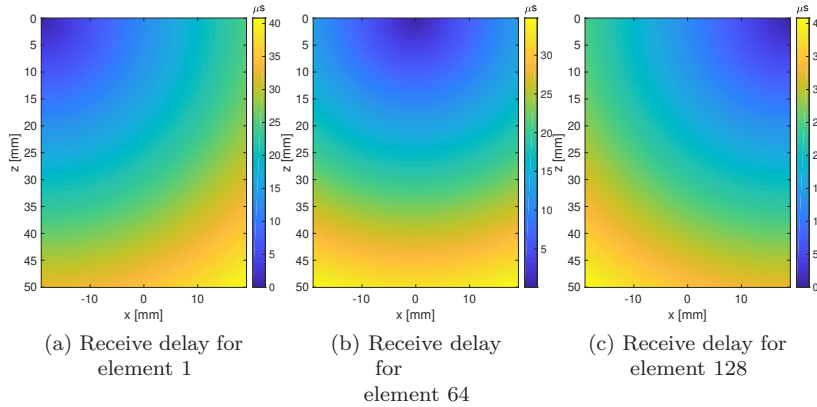


Figure 1.17: Receive delay for three different elements (a) the first element, (b) the 64th element and (c) the 128th element.

The transmit distance T is dependent on the type of transmit wave, and we will consider the four different types of transmit waves, as described in Section 1.5.

Transmit delay for Plane Waves (PW)

When one or multiple planar transmit beams are transmitted into the body at different transmit angles α , we are doing PW imaging (Montaldo et al., 2009). Then the transmit distance, T , becomes

$$T_{\text{PW}}(z, x, \alpha) = (z \cos(\alpha) + x \sin(\alpha)). \quad (1.16)$$

If we use the same scan and probe as earlier, the transmit delay for three different plane waves transmitted at -30° , 0° and 30° are visualized in Figure 1.18 using the same geometry as in Figure 1.17.

1. Scientific Background: Software Beamforming Methodology

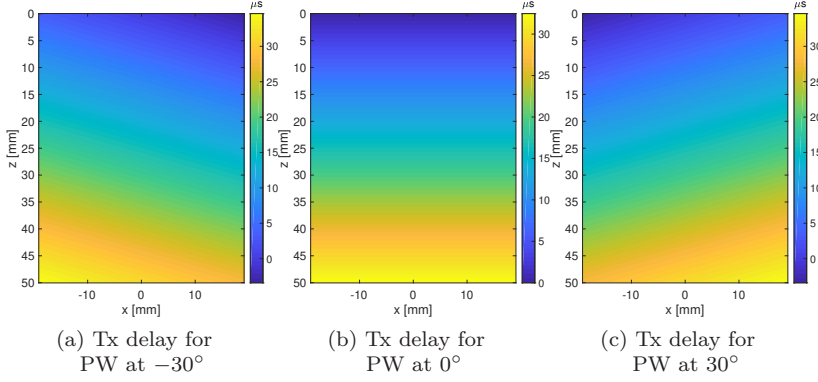


Figure 1.18: PW transmit delay for the full image scan for (a) a PW transmitted at -30° , (b) a PW transmitted at 0° , and (c) a PW transmitted at 30° .

Transmit delay for Diverging Waves (DW)

A diverging wave is formed by creating a virtual source behind the transducer at (x_s, z_s) with $z_s < 0$. The transmit distance, T , then becomes

$$T_{\text{DW}}(z, x, x_s, z_s) = \sqrt{(x - x_s)^2 + (z - z_s)^2}. \quad (1.17)$$

In Figure 1.17 we have plotted the transmit delay for three DWs using the same linear scan as earlier. Even though a diverging transmit wave is usually used with a sector scan, a linear scan was used for comparison to the earlier figures.

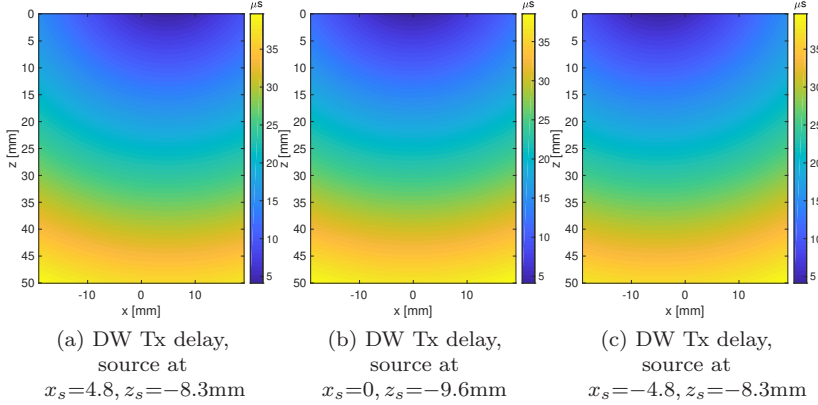


Figure 1.19: DW transmit delay for virtual source at (a) $x_s = 4.8, z_s = -8.3$ mm, (b) $x_s = 0, z_s = -9.6\text{mm}$ and (c) $x_s = -4.8, z_s = -8.3\text{mm}$.

Transmit delay for Synthetic Transmit Aperture Imaging (STAI)

The transmit delay for STAI images is the same as for a DW, but you place the source in the element firing. We can then assume $z_s = 0$ and that $x_s = x_m$

where x_m is the firing element. Thus, the transmit delay for STAI single firing element simplifies to the same as the receive delay in Figure 1.15.

Transmit delay for Focused Imaging (FI)

The transmit delay for software beamforming using Focused Imaging (FI) is actually a bit tricky. This is covered in detail in (Rindal, Rodriguez-Molares and Austeng, 2018). We will again borrow some text, with some slight modifications to the notation. Compared to (Rindal, Rodriguez-Molares and Austeng, 2018), we are changing from calculating the transmit time τ to the transmit distance T . The three different delay models for FI imaging; namely the spherical, the unified, and the hybrid delay model which we introduced in (Rindal, Rodriguez-Molares and Austeng, 2018), then becomes.

Spherical delay model

Using a simple spherical model (Nikolov, Kortbek and J. A. Jensen, 2010) the transmit distance is calculated as

$$T_{\text{FI spherical}} = |\vec{v}_k - \vec{x}_k| + |\vec{p} - \vec{v}_k|, \quad (1.18)$$

where \vec{v}_k denotes the location of the virtual source, \vec{x}_k is the center of the transmitting aperture, and $\vec{p} = (x, z)$ is the location of the pixel in the image.

The transmit distance has two terms: the travel distance from \vec{x}_k to \vec{v}_k , and the travel distance from \vec{v}_k to \vec{p} . If the reconstructed point, \vec{p} , is in front of the focal point, the second term will be negative, and otherwise positive. This scenario is illustrated by Figure 1.20.

By looking at the two terms we can see that at the focal depth, where the second term flips from negative to positive, we will get a discontinuity in the spherical transmit delay model.

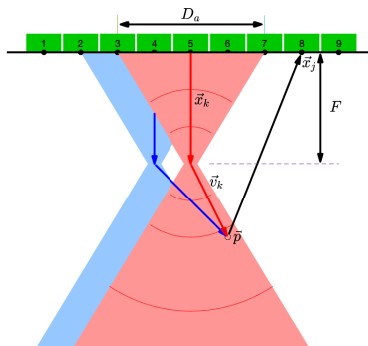


Figure 1.20: Delay geometry for a spherical virtual source as depicted in (Nikolov, Kortbek and J. A. Jensen, 2010). The blue and red indicate the insonified region from two individual transmits. Notice how they overlap in front of, and after the focal point at F . Figure credits to Andreas Austeng creating this figure from (Rindal, Rodriguez-Molares and Austeng, 2018).

“

Unified delay model

In (Nguyen and Prager, 2016) they analyzed and divided the transmitted wave field into four regions (I, II, III and IV) as seen in Fig. 1.21.

Their analysis showed that the transmitted signal is not a single pulse in regions II, and IV, but that it consists of two pulses that are comparable in strength. This violates the spherical wave assumption in regions II and IV, and the spherical transmit delay model is no longer valid.

As regions II and IV are not intensively insonified, the backscattered signal from these regions do not contribute significantly to the total beamformed energy. To correct the artifact (Nguyen and Prager, 2016) suggested to linearly interpolate the transmit distance between regions I and III, across regions II and IV, and weighting down the amplitude of the data from regions II and IV.

The unified delay model (Nguyen and Prager, 2016) then becomes

$$T_{\text{FI unified}} = \frac{|\vec{x}_b - \vec{p}|}{|\vec{x}_b - \vec{x}_a|} T_{\text{FI spherical},b} + \frac{|\vec{x}_a - \vec{p}|}{|\vec{x}_a - \vec{x}_b|} T_{\text{FI spherical},a}, \quad (1.19)$$

where \vec{x}_a and \vec{x}_b are vector positions of points A, B and \vec{p} is the reconstructed point as seen in Fig. 1.21. $T_{\text{FI spherical},a}$ and $T_{\text{FI spherical},b}$ are the distance calculated as in (1.18) for positions A and B.

”

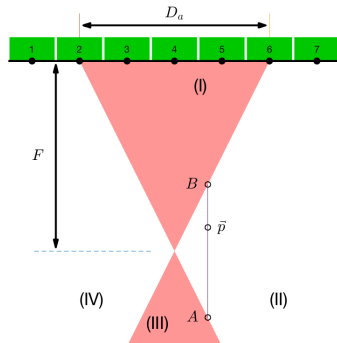


Figure 1.21: Delay geometry for the unified transmit delay model as described in (Nguyen and Prager, 2016). The wavefield is divided into four regions I, II, III and IV. Region I and III follows the spherical model, while the delay for a point \vec{p} in region II and IV is an interpolated value of the delay values in point A and point B. Figure credits to Andreas Austeng creating this figure for (Rindal, Rodriguez-Molares and Austeng, 2018).

“

Hybrid delay model

We present a hybrid transmit delay model combining features of spherical and plane waves. In essence, we assume that the transmit wave propagates as a plane-wave in a small region m around the transmit focus, yielding the

”

“

transmit distance

$$T_{\text{FI hybrid}} = \begin{cases} z, & \text{if } z > F_z - m \text{ and } z < F_z + m \\ T_{\text{FI spherical}}, & \text{otherwise.} \end{cases} \quad (1.20)$$

 where F_z is the focal depth.

”

The transmit delay, using a slightly deeper scan than earlier, for a focused transmission from the center of the array is, for all three models, plotted in Figure 1.22.

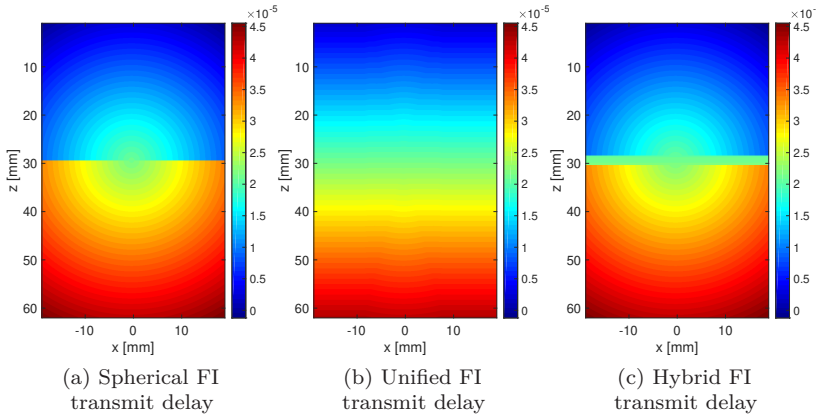


Figure 1.22: Transmit delays for a FI transmission from the center of the array using the (a) spherical, (b) the unified and (c) the hybrid transmit delay model. Figures from (Rindal, Rodriguez-Molares and Austeng, 2018).

We see that the spherical model has a discontinuity at the focus, $z = 29.6$ mm. The unified delay model does not have this discontinuity. The hybrid model "pushes" this discontinuity out of the focal zone in the lateral direction (x-direction). The discontinuity of the spherical model results in an artifact in the final image. Both the unified and hybrid model resolves this artifact - but the hybrid model is much less computationally expensive. Please see (Rindal, Rodriguez-Molares and Austeng, 2018) for more details, examples and in-depth discussion of this artifact. In the FI images in this chapter, such as in Section 1.5.4, we used the hybrid model.

1.7.2 The general beamformer – delay and sum

The conventional delay-and-sum (DAS) can be implemented using *the general beamformer*. The general beamformer makes "it [...] possible to beamform all sequences with a single algorithm" (Rodriguez-Molares, Rindal et al., 2017). The general beamformer can also, as we define it, reconstruct the image using channel data as either RF, IQ or as the analytical signal as described in Section 1.6. The DAS image is the coherent combination of the pixel values as received by all elements M from all transmits N_a . The subscript a denotes signal from

1. Scientific Background: Software Beamforming Methodology

each individual transmit, yielding

$$b_{\text{DAS}}(x, z) = \sum_{a=0}^{N_a-1} \sum_{m=0}^{M-1} w_a^{tx}(x, z) w_m^{rx}(x, z) s_{m,a}(x, z) e^{i2\pi f_{\text{demod}} \Delta t / f_s}. \quad (1.21)$$

Here w_m^{rx} is the receive apodization, see the details below, with dimensions $[N_z, N_x, M]$ while w_a^{tx} is the transmit apodization, see details in Section 1.7.4, with dimensions $[N_z, N_x, N_a]$.

If the channel data $s_{m,a}$ is the demodulated IQ-signal, we need to up-mix the signal by multiplying with $e^{i2\pi f_{\text{demod}} \Delta t / f_s}$. The demodulation frequency is f_{demod} , Δt is the delay from equation (1.13), and f_s is the sampling frequency. If we are beamforming using the RF signal or the analytical signal we can simply set the $f_{\text{demod}} = 0$ so that $e^{i2\pi f_{\text{demod}} \Delta t / f_s} = 1$.

For notational simplicity, let's rewrite (1.21). We will assume that we are using the analytical signal, and drop the spatial pixel coordinates (x, z) , such that

$$b_{\text{DAS}} = \sum_{a=0}^{N_a-1} \sum_{m=0}^{M-1} w_a^{tx} w_m^{rx} s_{m,a} = \sum_{tx} w_a^{tx} \sum_{rx} w_m^{rx} s_{m,a}. \quad (1.22)$$

Note also that we can define that the inner sum over the elements is the sum over the receive (rx) dimension, while the sum over the a transmits are the sum over the transmit (tx) dimension, and that we can move the transmit weights w_a^{tx} out of the inner sum. If we have a closer look on the delayed channel data in $s_{m,a}$ we can visualize the data from each transmit a as a three dimensional cube where the first dimension is the z 's, thus the depth pixels, the second dimension is the x 's and the third dimension is the receive elements m . Thus, $s_{m,1}$ have dimensions $[N_z, N_x, M]$ and we will have N_a of these cubes, one from each transmit a .

Receive Apodization

The receive apodization, using a uniform rectangular window, can be calculated as

$$w_m^{rx}(z, x, x_m) = \begin{cases} 1, & \text{if } |x - x_m| \leq \frac{z}{2f\#} \\ 0, & \text{otherwise.} \end{cases} \quad (1.23)$$

Here (x, z) is the pixel position, x_m is the position of the receiving element and $f\#$ is the f-number. The f-number is defined as $f\# = \frac{z}{D}$, the ratio between the pixel depth z and the size of the aperture D . This results in an expanding aperture with a constant f-number, as shown when we, in Figure 1.23a, plot the apodization for the L7-4 probe with depth for the center pixel line, $x \approx 0$ mm, when using $f\# = 1$. Other apodization window functions can be applied. One can use the expression in (1.23) to find the "active" elements and calculate the window based on the number of active elements. This is done for the Hamming window in Figure 1.23b. The choice of window function will, as is well known, influence the resolution and side lobe suppression.

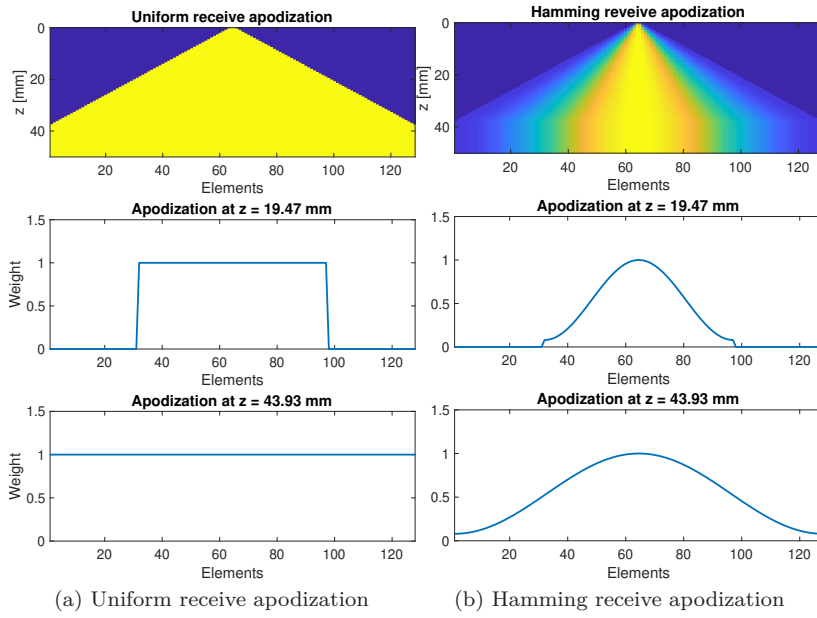


Figure 1.23: Receive apodization for the center pixel $x \approx 0$ mm for the L7-4 probe with depth when using $f\# = 1$. A uniform window is used in (a), while a Hamming window is used in (b).

1.7.3 Coherent compounding

We can split up the sum in equation (1.22) into two

$$b_a^{\overline{R}_{x\text{DAS}}} = \sum_{rx} w_m^{rx} s_{m,a} \quad (1.24)$$

$$b_{\text{DAS}} = b^{\overline{T}_{x\text{DAS}}} \overline{R}_{x\text{DAS}} = \sum_{tx} w_a^{tx} b_a^{\overline{R}_{x\text{DAS}}}. \quad (1.25)$$

Here $b_a^{\overline{R}_{x\text{DAS}}}$ is the result from the sum over the receive elements M , where we with the superscript $\overline{R}_{x\text{DAS}}$ denote that we have used a coherent combination of the signals over the receive dimensions, and equivalently that $\overline{T}_{x\text{DAS}}$ denotes a coherent combination over the transmit dimension. This is what is known as coherent compounding, extensively used with plane waves (Montaldo et al., 2009) and diverging waves (Papadacci et al., 2014). All techniques dependent on coherent compounding are affected by object movement between transmissions. If the object move between transmission this will degrade the synthetic focusing mechanism of compounding (Denarie et al., 2013). There exist many studies trying to compensate for this effect, however, we will for simplicity assume stationary targets.

1.7.4 Incoherent compounding

In contrast to the section above where we did a coherent combination of data, thus utilizing the constructive and non-constructive alignment of the signals,

1. Scientific Background: Software Beamforming Methodology

one can also do a incoherent combination of data. This means that we take the absolute value inside the sum of equation 1.25 so that we get

$$b_{\text{DAS tx incoherent}} = b^{\overline{T}_{x\text{DAS incoherent}} \overline{R}_{x\text{DAS}}} = \sum_{tx} |w_a^{tx} b_a^{\overline{R}_{x\text{DAS}}}|. \quad (1.26)$$

This is often used as part of speckle reduction techniques which we will not elaborate on here. However, see Section 1.10 for some more details on speckle and speckle statistics. The crucial point of the last two sections is that combining the complex data results in a coherent combination of signals utilizing constructive and non-constructive alignment of the signals resulting in e.g. improved resolution. While a incoherent combination, taking the absolute sign inside the sum, results in smoother speckle pattern but sacrifices resolution.

Transmit Apodization

The transmit apodization needs some explanation, since we in the USTB denote transmit apodization for the apodization applied over the transmit dimension of the received data, as defined in equation (1.22). The apodization applied over the elements when transmitting the ultrasound wave, we will denote transmit waveform apodization.

Transmit Angular Apodization

In (Rodriguez-Molares, Torp et al., 2015) the term angular apodization was coined to the apodization weights applied to the different single transmit low-quality plane wave images before coherent compounding. It was shown that CPWC imaging with angular apodization obtains the same image quality as STAI with apodization applied in the coherent compounding of the single transmit images and as FI with transmit waveform apodization. Thus, the results in (Rodriguez-Molares, Torp et al., 2015) shows that the transmit waveform apodization for FI imaging is connected with the angular transmit apodization applied to the receive data when synthetically creating a focus through coherent compounding.

Transmit Masking Apodization

A second type of transmit apodization is a masking apodization. Again, we are talking about transmit apodization as the apodization over the TX dimension of the received data as in equation (1.22). The masking apodization can be thought of as masking out the region insonified by the transmit beam. A good way of illustrating the region insonified is to view the single transmit B-mode image of a FI transmit. Three of these are shown in Figure 1.11.

We will consider three different imaging modalities for focused imaging which can all be viewed as a variant of transmit masking apodization. Namely, scan-line beamforming, multiple line acquisition (MLA) and retrospective beamforming (RTB).

1.7.5 Scan-line beamforming

Conventional scan-line beamforming, meaning one transmit beam resulting in one axial line in the image can be viewed as a transmit masking apodization.

1.7. Software Beamforming

The masking apodization is then to mask out everything except the single line in the single transmit B-mode image. This is demonstrated in Figure 1.24 (a) to (c), where we have plotted three of the 128 scan-lines constituting the final image in (d).

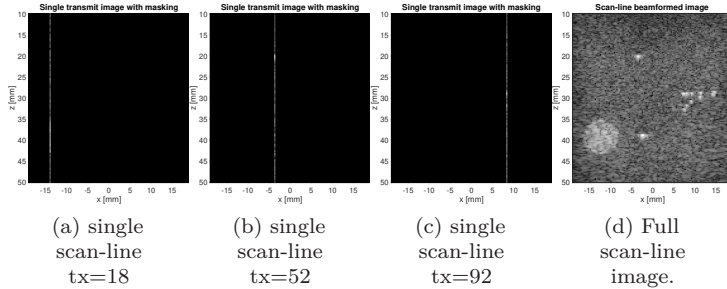


Figure 1.24: Conventional scan-line beamforming as implemented in the USTB software beamforming using apodization to make one beam from each transmit.

1.7.6 Multiple Line Acquisition

To increase the image quality, a common strategy is to acquire multiple receive lines for every line transmitted - resulting in what is known as a multiple line acquisition (MLA). Alternatively, one can reconstruct an image with fewer transmits using MLA. Conventionally, this has been known as parallel beamforming (Shattuck et al., 1984), or multiline beamforming. In the PW and DW case, thus broad transmit beams, MLA can easily be implemented in software beamforming by simply defining a suitable image scan of pixels. However, with focused transmissions the narrow insonified region around focus might lead to some unwanted effects known as beam warping and skewing. These effects have been described and discussed in detail in (Hergum et al., 2007). We will not touch the details here, but the unwanted effects result in amplitude variations in the image since the receive lines do not line up with the transmit beams. One solution is the Synthetic Transmit Beams (STB) technique introduced in (Hergum et al., 2007). The STB technique introduces "shift invariance through coherent interpolation". In our USTB software beamforming framework this means that we can implement the STB technique using coherent compounding of single transmit images. By using appropriate transmit apodization masking we can decide the number of synthetic lines and how much they should overlap between transmits. First, let us demonstrate extra parallel receive beams, but without doing any coherent compounding between the transmits. Figure 1.25 illustrates in the two left plots the masking apodization used for $tx = 100$ and $tx = 101$ respectively, and the corresponding single transmit images to the right.

To do coherent compounding, there needs to be some overlap between the single transmit images. Figure 1.26 demonstrates an example where we have used a total of 8 MLAs with two MLAs overlapping between each transmit. Again, the two left plots are the masking apodization used for $tx = 100$ and $tx = 101$ respectively, and the corresponding single transmit images to the right.

1. Scientific Background: Software Beamforming Methodology

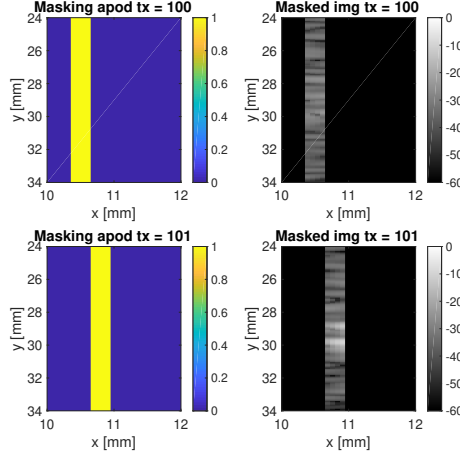


Figure 1.25: MLA beamforming with no overlap between the beams. Using 4 MLAs per beam with the transmit masking apodization in the left images, and the resulting single transmit images with the masking applied to the right.

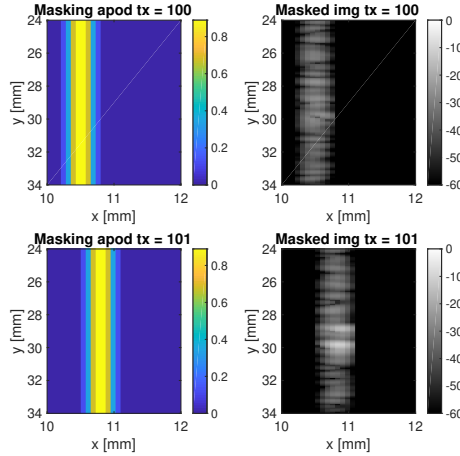


Figure 1.26: Transmit delays for a FI transmission from the center of the array using the (a) spherical, (b) the unified and (c) the hybrid transmit delay model.

From Figure 1.26 we can see how the two single transmit images now overlap and how the masking is created so that the amplitude in the overlapping region sums to 1.

The final images are shown in Figure 1.27 from the MLAs with no overlap to the left, and the MLAs with overlap to the right. Notice the striping artifacts in the left image, which is the image without overlap, and notice how the overlap between the transmit events smooths these striping artifacts out in the image to the right.

1.7.7 Retrospective Beamforming

By comparing the images with MLAs (Figure 1.27) to the conventional scan-line based image, we can see a clear improvement in the image quality. However,

1.7. Software Beamforming

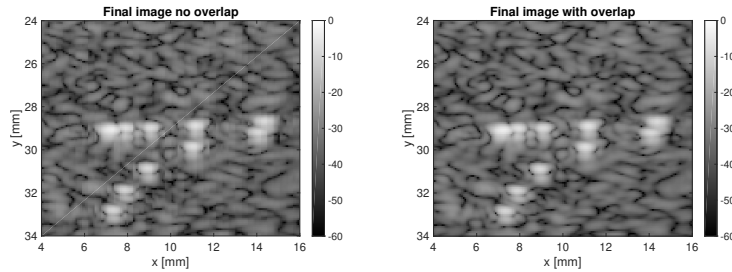


Figure 1.27: Final images created with MLAS with no overlap to the left, and with overlap to the right. Notice how the image with no overlap have some striping artifacts.

from the single focused transmit images in Figure 1.11, we can see that there is more than just a wide stripe that is insonified. The transmitted beam results in a converging shape before the focus, and a diverging shape after the focus. Thus, there is more than the "stripe" exploited in the MLA technique that overlaps between transmits. This brings us to, to the author's knowledge, the state of the art in terms of image quality; retrospective beamforming (RTB). The concept have been known for some time, and already in 1995 Freeman, P. C. Li and Odonnell published the paper titled Retrospective Dynamic Transmit Focusing. RTB has further been refined and is today considered a technique that uses a "virtual source" in focus (Frazier and O'Brien, 1998)(Bae, 2000)(Nikolov, Kortbek and J. A. Jensen, 2010). RTB imaging can also be implemented, as is done in the USTB, using the general beamformer and a transmit masking apodization. Figure 1.28 shows to the left a full FI single transmit image, and to the right, the same image but with a suitable transmit masking apodization applied. The transmit masking is masking out the part of the image that is insonified. We will not touch the details here. However, the calculation is based on the transmit foci and the number of active elements in the transmission.

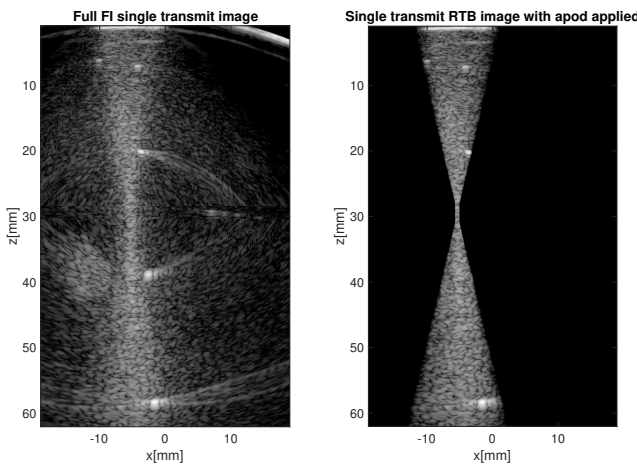


Figure 1.28: A full FI single Transmit image in (a) the same image in (b) with a suitable transmit masking apodization.

1. Scientific Background: Software Beamforming Methodology

The advantage of RTB imaging is that it combines the benefits from a focused transmission and the synthetic focusing achieved from coherent compounding.

Figure 1.29 shows three single transmit apodized images from transmit 47, 52, and 57, respectively. Notice, for example, how the point scatter at $z = 20\text{mm}$, $x = -2\text{mm}$ is visible in all three images, and thus is for all ten single transmit images between $tx = 47$ and $tx = 57$. The point scatterers deeper in the image will be insonified in even more transmits as the overlap region is largest away from the foci. Thus, there is a nice correlation between the number of overlapping transmits and how unfocused the transmit is.

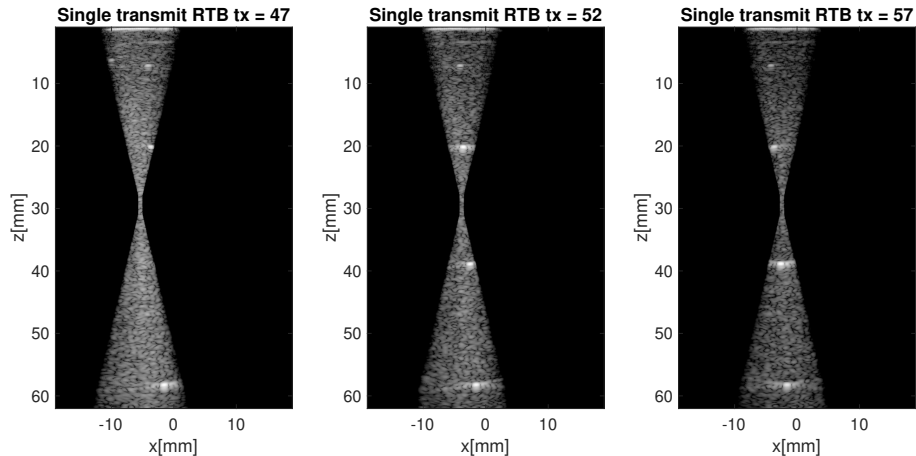


Figure 1.29: Three single transmit FI images with suitable transmit masking apodization.

Figure 1.30a is the resulting image from the coherent compounding of the masked single transmit RTB images. The lower amplitude in the focal region is because this region had the least number of overlaps. To compensate for the difference in amplitude, we apply an apodization based on the single transmit apodization masks. The final image is displayed in Figure 1.30b.

A comparison between the conventional scan-line beamforming, MLA beamforming and RTB beamforming is made in Figure 1.31. The images are created from the same channel data with the same number of transmits. For completeness, we also included an interpolated version of the scan-line beamformer to have the same number of pixels as for the MLA and RTB images. In Figure 1.31, we have zoomed in on the group of scatterers in the focal region. The B-mode image is shown in the top, while the lateral line through the scatterers is plotted below.

As expected, the MLA and RTB have some improved resolution, in terms of increased separability between the two leftmost scatterers. The difference between MLA and RTB is minimal. This is as expected, since these scatterers are located close to the foci where the MLA is already quite optimal.

However, in Figure 1.32 we investigate a point scatterer further away from the foci. From the B-mode images, and especially the plot of the axial line, we can observe that RTB resulted in an improved resolution. The improved resolution is because the coherent compounding in the overlapping regions of

1.7. Software Beamforming

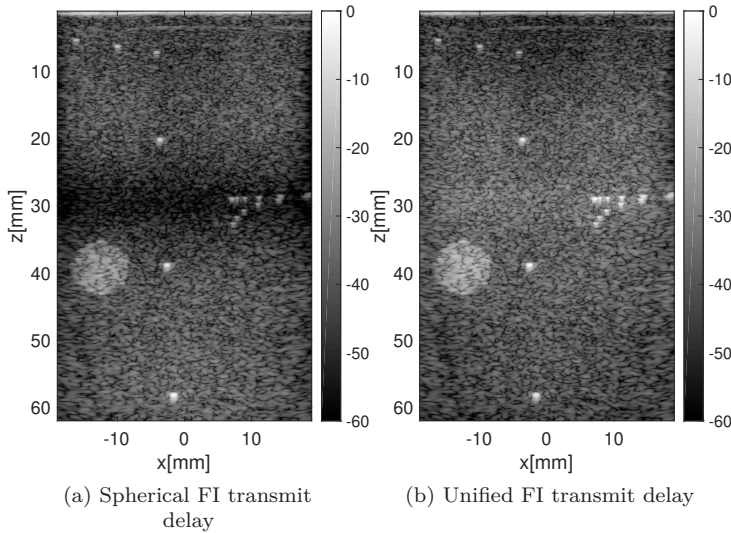


Figure 1.30: (a) is the resulting image from the coherent compounding of the transmit masked single transmit RTB images. The lower amplitude in the focal region is because this region had the least number of overlaps. To compensate for the difference in amplitude, we apply an apodization based on the single transmit apodization masks. The final image is displayed in Figure (b)

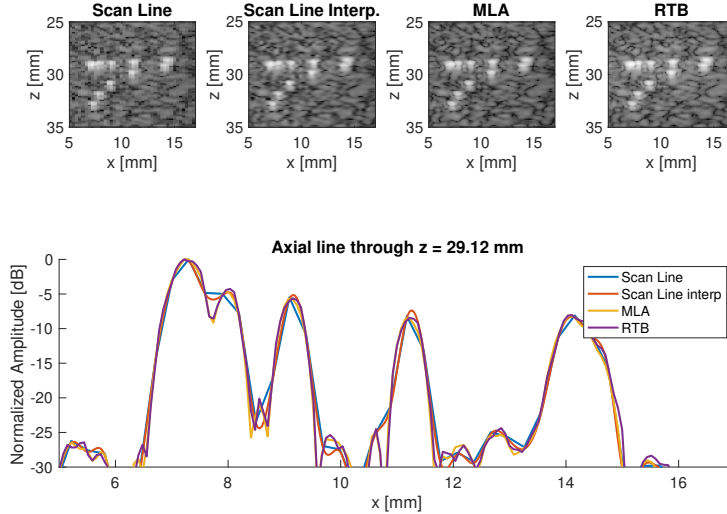


Figure 1.31: The conventional scan-line image in the top left, followed by an interpolated version of the scan-line image, the MLA image and the RTB image. The plot below is the axial line through the group of scatterers close to the foci.

RTB resulted in an improved synthetic resolution for the RTB. Also, notice the improved side-lobe levels.

1. Scientific Background: Software Beamforming Methodology

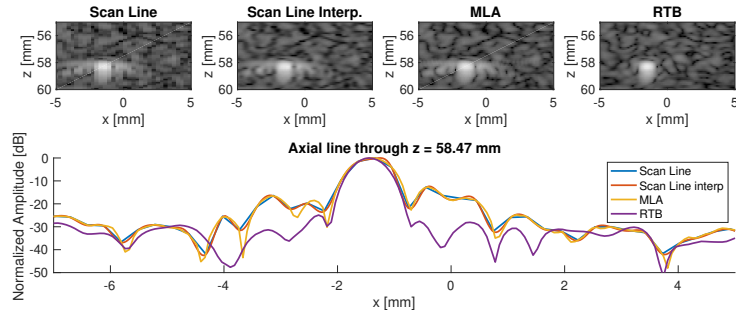


Figure 1.32: The conventional scan-line image in the top left, followed by an interpolated version of the scan-line image, the MLA image and the RTB image. The plot below is the axial line through the single scatterer almost 30 mm below the foci.

1.8 Adaptive beamforming

Most of the work in this thesis regards the image quality resulting from adaptive beamfoming ((Rindal and Austeng, 2016), (Prieur, Rindal and Austeng, 2018), (Rindal, Rodriguez-Molarez and Austeng, 2017), (Rindal, Austeng et al., 2019), (Hverven et al., 2017), (Rodriguez-Molarez et al., 2019) and (Rindal, Aakhus et al., 2017)). We will reuse a compact definition and introduction to adaptive beamforming from (Rindal, Austeng et al., 2019):

“

The popularization of software beamforming has brought numerous techniques that, by clever manipulation of channel data, are able to exceed the contrast and resolution provided by conventional delay-and-sum (DAS) beamforming. We refer as adaptive beamforming to any technique where the signal values alter the way the beamformed signal is constructed, for instance when the element weights are determined from the variance of the signal.

Seminal work on adaptive beamforming dates back to the 1960s, where optimal element weights were derived for a given signal direction to minimize the influence of jamming signals in radio communication systems (Applebaum, 1976; Bryn, 1962; Capon, 1964; Widrow et al., 1967).

Adaptive beamforming was first applied to medical ultrasound at the end of the 1980s to compensate for phase aberration artifacts produced by tissue inhomogeneities (Flax and O’Donnell, 1988; Nock, Trahey and S. W. Smith, 1989), and about a decade later to reduce the contribution of off-axis targets (Mann and W. F. Walker, 2002; Sasso and Cohen-Bacrie, 2005; J. Synnevåg, Austeng and Holm, 2005; Viola and W. Walker, 2005; Wang, J. Li and Wu, 2005).

”

There is a myriad of techniques that are published within the field of adaptive beamforming for medical ultrasound imaging. We have implemented some of the most popular ones in the USTB. Quite some effort was spent in **Paper VII** to formulate a compact description of these adaptive beamformers. We will, therefore, reuse the formulation here. For simplicity, compared to (1.21), we will assume only one transmit and drop the subscript a when defining the adaptive beamformers, so that $s_m(x, z)$ means the signal received on element

m for pixel location (x, z) .

1.8.1 Capon's Minimum Variance (MV)

Capon's Minimum Variance (MV) technique calculates a data dependent set of weights \mathbf{w} while maintaining unity gain in the steering direction (J.-F. Synnevåg, Austeng and Holm, 2009). This is posed as a minimization problem by

$$\begin{aligned} \min_{\mathbf{w}} E \{ |b_{\text{DAS}}|^2 \} &= \mathbf{w}^H \mathbf{R} \mathbf{w} \\ \text{subject to } \mathbf{w}^H \mathbf{a} &= 1, \end{aligned} \quad (1.27)$$

where $\mathbf{R} \equiv E \{ \mathbf{s} \mathbf{s}^H \}$ is the spatial covariance matrix, E is the expected value operator, and the steering vector $\mathbf{a} = \mathbf{1}$ because it is assumed that all signals are already delayed. The solution to (1.27) can be found by the method of Lagrange multipliers, yielding

$$\mathbf{w}_{\text{MV}} = \frac{\mathbf{R}^{-1} \mathbf{a}}{\mathbf{a}^H \mathbf{R}^{-1} \mathbf{a}}. \quad (1.28)$$

The spatial covariance matrix is unknown, but it can be estimated for point (x, z) , assuming a linear array, by (J.-F. Synnevåg, Austeng and Holm, 2009)

$$\hat{\mathbf{R}}(x, z) = \frac{\sum_{k=-K}^K \sum_{l=0}^{M-L} \bar{\mathbf{s}}_l(x, z - k) \bar{\mathbf{s}}_l^H(x, z - k)}{(2K+1)(M-L+1)}, \quad (1.29)$$

where $(2K + 1)$ is the number of axial samples, L is the length of the subarray, and

$$\bar{\mathbf{s}}_l(x, z) = [s_l(x, z) \ s_{l+1}(x, z) \ \dots \ s_{l+L-1}(x, z)]^T. \quad (1.30)$$

The subarray averaging improves robustness. To further improve robustness, and numerical stability, diagonal loading is added to the estimated covariance matrix by $\tilde{\mathbf{R}}(x, z) = \hat{\mathbf{R}}(x, z) + \epsilon \mathbf{I}$, where \mathbf{I} is the identity matrix, and

$$\epsilon = \frac{\Delta}{L} \text{tr}\{\hat{\mathbf{R}}(x, z)\},$$

where $\text{tr}\{\}$ is the trace operator.

The beamformed image is then computed as

$$b_{\text{MV}} = \frac{1}{M - L + 1} \sum_{l=0}^{M-L} \mathbf{w}_{\text{MV}}^H \bar{\mathbf{s}}_l. \quad (1.31)$$

1.8.2 Eigenspace-Based Minimum Variance (EBMV)

The MV can be extended into EBMV. Asl and Mahloojifar, 2010 was the first to apply it to beamforming for medical ultrasound. They utilized the eigenstructure of the covariance matrix aiming to obtain a better suppression of off-axis signals. The covariance matrix is estimated with (1.29) and eigendecomposed as

$$\hat{\mathbf{R}}_{\text{DL}} = \mathbf{V} \Lambda^{-1} \mathbf{V}^H, \quad (1.32)$$

‘‘

where $\Lambda = [\lambda_1, \lambda_2, \dots, \lambda_L]^T$ are the eigenvalues in descending order, and $\mathbf{V} = [\mathbf{v}_1, \mathbf{v}_2, \dots, \mathbf{v}_L]$ are the corresponding eigenvectors. The signal subspace \mathbf{E}_s can be constructed using the eigenvectors corresponding to the largest eigenvalues,

$$\mathbf{E}_s = [\mathbf{v}_1, \dots, \mathbf{v}_E], \quad (1.33)$$

where E is the number of eigenvectors creating the signal subspace. Finally, the EBMV weight is obtained by projecting the conventional MV weights onto the constructed signal subspace

$$\mathbf{w}_{\text{EBMV}} = \mathbf{E}_s \mathbf{E}_s^H \mathbf{w}_{\text{MV}}. \quad (1.34)$$

The beamformed image is then computed as

$$b_{\text{EBMV}} = \frac{1}{M-L+1} \sum_{l=0}^{M-L} \mathbf{w}_{\text{EBMV}}^H \bar{\mathbf{s}}_l, \quad (1.35)$$

with $\bar{\mathbf{s}}_l$ defined as in (1.30).

1.8.3 Filtered-delay-multiply-and-sum (F-DMAS)

F-DMAS for medical ultrasound beamforming was introduced in (Matrone, Savoia and Magenes, 2015). The technique aims to increase image quality by multiplying the RF signals before summation. Namely, the signed square root signal is defined as

$$g_{ij} = \text{sign}(s_i s_j) \sqrt{|s_i s_j|}, \quad (1.36)$$

where $\text{sign}(\cdot)$ denotes the sign function. The beamformed signal $b_{\text{F-DMAS}}$ is then computed as

$$b_{\text{F-DMAS}} = \left[\sum_{i=0}^{M-2} \sum_{j=i+1}^{M-1} g_{ij} \right]_{\text{BPF}}, \quad (1.37)$$

where $[\cdot]_{\text{BPF}}$ denotes the band pass filtering of the signal inside the brackets. Note that (1.36) is the multiplication of two signals with identical center frequency f_c , and hence it will have two frequency components: one at 0, and one at $2f_c$. Band pass filtering is applied to remove the DC component.

1.8.4 Coherence Factor (CF)

The CF was first introduced in (Mallart and Fink, 1994), as the ratio between the coherent and incoherent energy across the aperture:

$$\text{CF} = \frac{\left| \sum_{m=0}^{M-1} s_m \right|^2}{M \sum_{m=0}^{M-1} |s_m|^2}. \quad (1.38)$$

’’

“

The CF has been used as an adaptive weight to increase image quality (P. C. Li and M. L. Li, 2003) as;

$$b_{\text{CF}} = \text{CF } b_{\text{DAS}}. \quad (1.39)$$

1.8.5 Generalized Coherence Factor (GCF)

In (P. C. Li and M. L. Li, 2003) they generalized the coherence factor as

$$\text{GCF} = \frac{\sum_{n=-\frac{M}{2}}^{\frac{M}{2}-1} |S_n|^2}{\sum_{n=-\frac{M}{2}}^{\frac{M}{2}-1} |S_n|^2}, \quad (1.40)$$

where S is the M -point Fourier spectra over the aperture of the delayed channel data,

$$S_n = \sum_{m=0}^{M-1} s_m e^{-j2\pi(m-M/2)d\frac{n}{Md}}, \quad (1.41)$$

where $n \in [-\frac{M}{2}, \frac{M}{2}-1]$ is the spatial frequency index where M is assumed to be even, d is the pitch of the array, and M_0 is an arbitrary constant within $[0, \frac{M}{2}-1]$ that specifies the low spatial frequency region, thus going from $-M_0$ to M_0 . Note that if $M_0 = 0$ the GCF simplifies to the CF.

The beamformed image is computed by multiplying the DAS image with GCF

$$b_{\text{GCF}} = \text{GCF } b_{\text{DAS}}. \quad (1.42)$$

1.8.6 Phase Coherence Factor (PCF)

The PCF was introduced in (Camacho, Parrilla and Fritsch, 2009) as

$$\text{PCF} = \max \left\{ 0, 1 - \frac{\gamma}{\sigma_0} p \right\}, \quad (1.43)$$

where γ is a parameter to adjust the sensitivity of PCF to out-of-focus signals, $\sigma_0 = \pi/\sqrt{3}$ is the nominal standard deviation of a uniform distribution between $-\pi$ and π , and p is given by

$$p = \min \{ \sigma(\phi), \sigma(\phi^A) \}, \quad (1.44)$$

where $\phi = [\phi_1 \ \phi_2 \dots \phi_M]$ is the instantaneous phase across the aperture, and $\sigma(\phi)$ is its standard deviation. To avoid phase wrapping discontinuity a set of auxiliary phases $\phi^A = [\phi_1^A \ \phi_2^A \dots \phi_M^A]$ is computed as

$$\phi_m^A = \begin{cases} \phi_m + \pi & \text{if } \phi_m < 0, \\ \phi_m - \pi & \text{otherwise.} \end{cases} \quad (1.45)$$

The beamformed image is computed using PCF as an adaptive weight

$$b_{\text{PCF}} = \text{PCF } b_{\text{DAS}}. \quad (1.46)$$

”

1.8.7 Short Lag Spatial Coherence (SLSC)

In addition to the adaptive beamformers mentioned so far, this thesis includes a study including the Short Lag Spatial Coherence (SLSC) in (Rodriguez-Molarez et al., 2019). For completeness, we will, therefore, include a definition here. The short lag spatial coherence (SLSC) algorithm was introduced in (Lediju et al., 2011). The spatial correlation can be calculated as

$$\hat{R}(m) = \frac{1}{M-m} \sum_{i=1}^{M-m} \frac{\sum_{n=n_1}^{n_2} p_i(n)p_{i+m}(n)}{\sqrt{\sum_{n=n_1}^{n_2} p_i^2(n)p_{i+m}^2(n)}}, \quad (1.47)$$

where p is the delayed signal, n is the depth sample index, m is the distance, or lag, in number of elements between two point on the aperture. The sum over n results in a correlation over a given kernel size, $n_2 - n_1$ of pixels. The short lag spatial coherence, is calculated as the sum over the first M lags,

$$b_{\text{SLSC}} = \sum_M^M \hat{R}(m). \quad (1.48)$$

Thus, notice that b_{SLSC} is an image of the coherence and not the backscattered signal amplitude as with DAS and MV. The SLSC is a visualization of the spatial coherence of backscattered ultrasound waves, building upon the theoretical prediction of the van Cittert-Zernike (VCZ) theorem . The implications of the VCZ theorem for pulse-echo ultrasonic imaging was discussed by Mallart and Fink, 1991; Mallart and Fink, 1994.

Some of the adaptive methods have user settable parameters. For the results presented in this chapter we used the same parameteres as in (Rindal, Rodriguez-Molarez and Austeng, 2017).

“

For MV, L was set to 50% of the active receive channels, $K = 1.5\lambda$, and a diagonal loading factor of $\Delta = 1/100$ was used as suggested in (J.-F. Synnevåg, Austeng and Holm, 2009). The number of eigenvectors used in EBMV was selected adaptively using the eigenvectors with eigenvalues larger than $\delta = 0.5$ times the maximum eigenvalue as suggested in (Asl and Mahloojifar, 2010). For GCF the value $M_0 = 2$ was used as suggested in (P. C. Li and M. L. Li, 2003). For PCF $\gamma = 1$ was chosen as suggested in (Camacho, Parrilla and Fritsch, 2009).

”

1.8.8 Categorizing adaptive beamformers

With the myriad of adaptive techniques, a way of categorizing them could be useful. We will suggest two different categorizations.

Categorization I : Coherence and non-coherence adaptive beamforming

Coherence F-DMAS, CF, GCF, PCF and SLSC

Non-coherence MV and EBMV.

The first categorization is based on if the beamformers exploit the coherence, or in a more general term similarity, of the wavefront received over the aperture. The connection between F-DMAS and coherence is not obvious. However, in (Prieur, Rindal and Austeng, 2018) we studied this in detail and concluded that "Being largely influenced by the signal coherence, the F-DMAS beamformer appears as an intermediate between the DAS beamformer and beamformers using coherence factor weighting". The CF, GCF, and PCF all weight the DAS image with a weight directly dependent on the signal coherence. In CF this is calculated from the signal directly. In GCF as a generalization of the CF through the Fourier spectra over the aperture. In PCF the coherence is measured as similarity based on the standard deviation of the phase over the aperture. The SLSC calculates the coherence based on a normalized correlation of the signal over the aperture. The MV and EBMV, on the other hand, are calculating an adaptive weight set that is trying to suppress unwanted off-axis signals based on the minimization problem posed. Thus, they are not "measuring" the coherence as the other beamformers, and we categorize them as non-coherence beamformers.

Categorization II : Adaptive element vs adaptive image weights

Element weights MV, EBMV, and F-DMAS

Image weights CF, GCF and PCF.

The second categorization is based on where the "adaptiveness" is applied. Both the MV and EBMV calculate an adaptive weight set that is applied in the summation of the signal. The F-DMAS does not calculate a weight set directly, but we will consider weighting the element signals with each other as some kind of element weighting.

The CF, GCF, and PCF are all weighting the DAS image with an *image weight* based on some coherence estimate, and thus, the adaptiveness is applied as an image weighting. The issue with categorization II is that the SLSC does not fit within this definition of categories since it displays the coherence directly and not multiplied with the image.

There do exist publications where adaptive methods are combined across these categories. For example, when coherence image weights are applied as a weighting to MV images (Chau, Lavarello and Dahl, 2016), thus there truly is a myriad of adaptive beamformers.

1.9 Post processing

Whether we have the image b_{DAS} created by the conventional DAS image as in equation (1.21). Or we have an image created by an adaptive beamformer such as the b_{MV} from the minimum variance beamformer equation (1.31), there are some final stages before the image is displayed on the screen.

1.9.1 Detecting the envelope

From Section 1.6, we know that if we have the analytical signal or the IQ-signal we can simply detect the envelope A of the signal by taking the absolute value

$A = |b|$, where b for example is b_{DAS} from equation (1.21). If we have used the RF signal through the beamforming chain, the envelope can be detected by generating the analytical signal of the beamformed data, b . Thus, creating a complex signal by using the Hilbert transform of the data as the imaginary component. However, the number of pixels in the axial (z) direction is then very important. The signal in the axial direction needs to be well sampled to avoid artifacts in the image introduced from the Hilbert transform. The number of samples in the axial direction (z) can be reduced if one uses the analytical signal through the processing chain, since the Hilbert transform is then taken on the well sampled RF channel data. The number of axial pixels can also be reduced if one uses the IQ-signal.

1.9.2 Log compression

Ultrasound images are, at least in the research literature, usually shown in a logarithmic scale. Thus, the final stage is to do a logarithmic compression of, for example, the DAS signal so that

$$B_{\text{DAS}} = 20 \log_{10}(A_{\text{DAS}}) = 20 \log_{10}(|b_{\text{DAS}}|), \quad (1.49)$$

where A_{DAS} is the signal envelope and b_{DAS} (assuming IQ or analytical signal) is the coherent combination of the delayed signals as described in equation (1.21). The exception from the log compression is for example SLSC images that are for some applications shown in the natural scale (Lediju Bell et al., 2013). The SLSC image is an image of the coherence directly.

1.9.3 The dynamic range

The logarithmically compressed images are often normalized so that the maximum value in the image is displayed as 0 dB. The dynamic range of the image is then the lowest value displayed in the image. A common dynamic range is from 0 dB to -60 dB, resulting in an image as displayed in Figure 1.33a. In Figure 1.33b, we have displayed the same image but using a dynamic range of 0 dB to -40 dB. The two images are an illustration of how simply changing the dynamic range can result in an image where the apparent contrast, in terms of the hypoechoic cyst, seems to be improved. (Rindal, Austeng et al., 2019) is an in-depth investigation into the effects adaptive beamforming has on the dynamic range with emphasis on how this affects the estimated contrast.

1.9.4 Further post processing

In a clinical scanner, the final stages of the processing chain of a B-mode ultrasound image would now contain different image processing algorithms, such as speckle reduction. We will, however, stop our description of the medical ultrasound processing chain here.

1.10 Speckle statistics

If we are imaging a scene of enough randomly distributed small scatterers reflecting the transmitted ultrasound wave, see Section 1.3, the resulting image

1.10. Speckle statistics

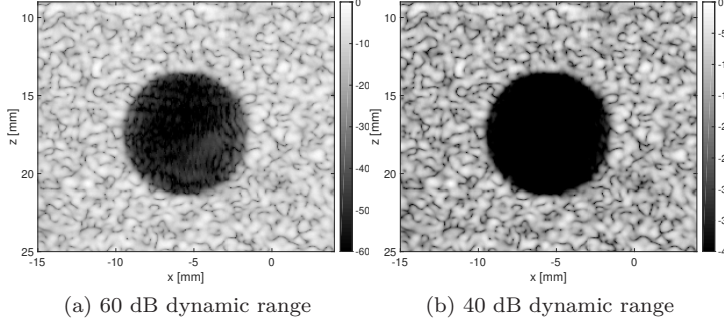


Figure 1.33: Two images illustration how changing the dynamic range can result in an image where the apparent contrast, in terms of the hypoechoic cyst, seems to be improved. (a) have 60 dB dynamic range, while (b) have 40 dB dynamic range. Data from (Rindal, Austeng et al., 2019).

is of a *speckle pattern*. The speckle pattern is considered to be *well developed* if the number of scatterers per resolution cell is larger than 10 (Wagner et al., 1983). An image simulated in Field II (J. A. Jensen, 1996; J. A. Jensen and Svendsen, 1992) of such a scenario is shown in Figure 1.34, with a few tricks to obtain a uniform field of view detailed in (Rindal, 2018).

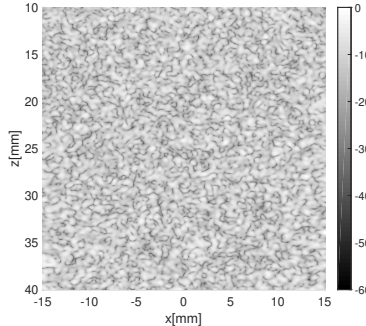


Figure 1.34: A STAI image of well developed speckle simulated in Field II.

According to (Wagner et al., 1983), well developed speckle results in an ultrasound pressure field that are circular Gaussian or more precisely a circularly-symmetric Normal distribution. This means that e.g. the analytical signal, both the real and imaginary parts, will follow a normal Gaussian distribution. This is confirmed in Figure 1.35, where we see that the estimated PDF for both the real and imaginary parts of the signal follows the theoretical normal Gaussian distribution.

The amplitude of the envelope follows a Rayleigh distribution with the theoretical probability function (Wagner et al., 1983)

$$f_{\text{Rayleigh}} = \frac{A}{\beta^2} e^{\frac{-A^2}{2\beta^2}}, \quad (1.50)$$

where A is the envelope amplitude and β is the scaling parameter than can be found from the variance of a Rayleigh distribution $\sigma^2 = \frac{4-\pi}{2}\beta^2$. The signal to

1. Scientific Background: Software Beamforming Methodology

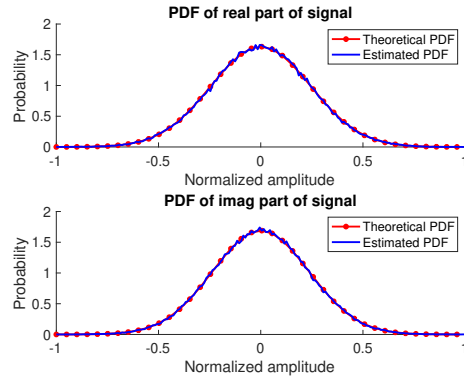


Figure 1.35: Estimated PDF of the real and imaginary part of the analytical signal plotted together with the theoretical normal Gaussian distribution.

noise ratio, $\text{SNR} = \frac{\mu}{\sigma} = 1.91$, where μ is the mean of the envelope, and σ is the standard deviation. The estimated SNR of the image in Figure 1.34 was 1.91 fitting the theoretical distribution very well, as we can see from Figure 1.36. Here we have plotted the estimated PDF together with the theoretical Rayleigh distribution. The Rayleigh distribution belongs to the family of Rician distributions.

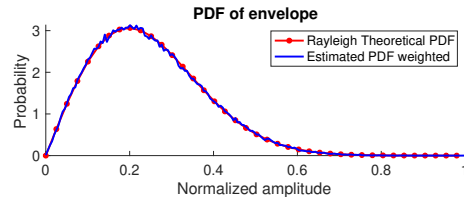


Figure 1.36: The estimated PDF of the envelope together with the theoretical Rayleigh distribution.

It is worth to mention that it is seldom large enough uniform areas in the body to create the well developed speckle. Often stronger targets or specular reflections will occur and result in different statistical distributions. However, for example the thyroid and the blood is known for having well developed speckle patterns.

The image in Figure 1.34 was created by the conventional DAS beamformer. In (Hverven et al., 2017), we investigated the speckle statistics of several adaptive beamformers and the influence on conventional contrast metrics. We showed that most adaptive beamformers do not follow the same speckle statistics as DAS. In (Prieur, Rindal and Austeng, 2018) the image amplitude and speckle statistics of the F-DMAS beamformer were investigated in detail. In (Rodriguez-Molarez et al., 2019), we argue that the alteration of the speckle statistics by adaptive beamformers is invalidating the conventional contrast metrics. We also use the known speckle statistics of DAS to derive analytical expressions of the contrast metrics for DAS.

1.11 Evaluation of image quality – metrics

By being introduced to the myriad of adaptive beamformers, we might have gained some insight into the author's motivations for using the word *curse* in the title of this thesis. The *curse*, in the author's opinion, is that software beamforming is so flexible that algorithms mostly optimizing the evaluation metrics, may be developed. More specifically, we, quite baldly, claim in (Rindal, Austeng et al., 2019) that "The results presented here expose a dangerous weakness of our image quality metrics. This weakness must be remediated. We must lay the groundwork upon which we build the new techniques. A new metric for contrast must be sought, one that is immune to dynamic range transformations, and help us assess the relevance of present and future beamforming techniques."

To understand how we got there, let's first have a look at the contrast metrics commonly used in ultrasound imaging.

1.11.1 Contrast

In (Rindal, Austeng et al., 2019), we summarized the current status of contrast measurements in ultrasound images:

No clear consensus exists yet on how to measure the contrast of ultrasound images. Perhaps the most widespread definition (Lediju et al., 2011; Matrone, Savoia and Magenes, 2015; Zhao et al., 2017) is the one in (S. Smith, Lopez and Bodine, 1985),

$$CR = \frac{\mu_{ROI}}{\mu_B}, \quad (1.51)$$

where $\mu = E\{|b|^2\}$ is the expected value of the power of the beamformed signal, in linear scale, over a certain region; and where ROI and B denote, respectively, a region of interest and a background region. If the signal power is proportional to the back-scattering coefficient, which is the case for speckle signals beamformed with DAS, then CR is proportional to the ratio of the particle concentration in both regions. CR, often referred to as contrast ratio, can be expressed in logarithmic scale as,

$$CR[dB] = 10 \log_{10} CR. \quad (1.52)$$

Detection probability not only depends on the mean value of the signal power but also on its variance. An alternative measure of contrast can be found in (Patterson and Foster, 1983), a measure that became later known as the contrast-to-noise ratio

$$CNR = \frac{|\mu_{ROI} - \mu_B|}{\sqrt{\sigma_{ROI}^2 + \sigma_B^2}}, \quad (1.53)$$

where $\sigma = \sqrt{E\{(|b|^2 - \mu)^2\}}$ is the standard deviation of the power of the beamformed signal, in linear scale. CNR is an estimate of the detection probability of a lesion. In particular for the case of circularly-symmetric Gaussian distributed signals, which is the case of speckle signals beamformed with DAS, CNR is bounded to the interval [0, 1]. This metric has been used

1. Scientific Background: Software Beamforming Methodology

“

by many authors (Lediju et al., 2011; Matrone, Savoia and Magenes, 2015; Shin and Huang, 2017; Zhao et al., 2017).

Even though the expressions (1.51) and (1.53) were originally proposed to be applied to signal power in natural units, many authors have chosen to insert log-compressed values in them, effectively defining the alternative metrics:

$$\text{CR}_{\text{LC}}[\text{dB}] = |\tilde{\mu}_{\text{ROI}} - \tilde{\mu}_{\text{B}}|, \quad (1.54)$$

where $\tilde{\mu} = E\{20 \log_{10}(|b|)\}$ is the expected value of the log-compressed values within the ROI and B region, and

$$\text{CNR}_{\text{LC}}[\text{dB}] = \frac{|\tilde{\mu}_{\text{ROI}} - \tilde{\mu}_{\text{B}}|}{\sqrt{\tilde{\sigma}_{\text{ROI}}^2 + \tilde{\sigma}_{\text{B}}^2}}, \quad (1.55)$$

where $\tilde{\sigma} = \sqrt{E\{(20 \log_{10}(|b|) - \tilde{\mu})^2\}}$ is the standard deviation of the log-compressed signal within the ROI and B region. We include the subindex LC to denote the metrics computed on log-compressed values.

Although (1.54) is similar to (1.52), they are not identical since $10 \log_{10}(E\{|b|^2\}) \neq E\{20 \log_{10}(|b|)\}$. CNR and CNR_{LC} take completely different values, and cannot be directly compared. Although both are thought to be estimates of the lesion detection probability, CR_{LC} can take values larger than 1, even for speckle signal beamformed with DAS. Several authors (Asl and Mahloojifar, 2010; Krishnan, Rigby and O'Donnell, 1997; Mehdizadeh et al., 2012; Nguyen and Prager, 2018; Shin and Huang, 2017) have chosen (1.54) and (1.55) to quantify contrast.

In some articles (Camacho, Parrilla and Fritsch, 2009; P. C. Li and M. L. Li, 2003; Ozkan, Vishnevsky and Goksel, 2018; Szasz, Basarab and Kouamé, 2016; Zhao et al., 2017; Zhuang, Rohling and Abolmaesumi, 2018) it is not explicit whether logarithmic or natural units have been used. In some others variations of the classical definitions are used (Asl and Mahloojifar, 2010; Krishnan, Rigby and O'Donnell, 1997; Ozkan, Vishnevsky and Goksel, 2018).

”

The consequences of the lack of consensus on how to measure ultrasound images are discussed in detail in (Rindal, Rodriguez-Molarez and Austeng, 2017), (Rindal, Austeng et al., 2019), (Hverven et al., 2017) and (Rodriguez-Molarez et al., 2019). Where we claim that adaptive beamformers are invalidating the conventional contrast metrics, which can be seen as one of the *curses* of software beamforming. Fortunately, a remedy to the *curse* is presented in (Rodriguez-Molarez et al., 2019) where we present an improved contrast metric immune to the unwanted effects from adaptive beamformers, namely the generalized contrast-to-noise ratio (GCNR).

1.11. Evaluation of image quality – metrics

1.11.2 Resolution

For completeness, we will have a brief look at how the resolution is evaluated in the medical ultrasound research literature. There exist multiple definitions of resolution ranging from the -3dB Rayleigh resolution criteria (Rayleigh, 1879), to the Sparrow resolution defined as where the saddle point between the two peaks first develops - thus being a measure on separability. A brief review shows that many authors tend to use the FWHM (-6 dB) (Liebgott et al., 2016; Matrone, Savoia and Magenes, 2015), while others use some measure of separability (Camacho, Parrilla and Fritsch, 2009; A. Jensen and Austeng, 2014) while some use both (Diamantis et al., 2019). We will have a brief look at both.

1.11.3 Resolution as the width of the point spread function

To measure resolution the convention is to image a single scatterer, resulting in an image of the point spread function (PSF) of the system and measure the full width half maximum (FWHM). The FWHM is equivalent to measuring the mainlobe width of the PSF at ≈ 6 dB. In Section 1.4, we saw how the FWHM made perfect sense when comparing the resolution between a wide linear array and a narrower phased array. However, the FWHM is often used to evaluate the resolution of adaptive beamformers, and we will look into some consequences.

In Figure 1.37, we have plotted the mainlobe of the PSF resulting from all the adaptive beamformers mentioned in Section 1.8, except SLSC. We have simulated a single point scatterer in Field II (J. A. Jensen, 1996; J. A. Jensen and Svendsen, 1992) illuminated by a single plane wave. The measured FWHM is indicated above the plot of the mainlobe, and in the bars below.

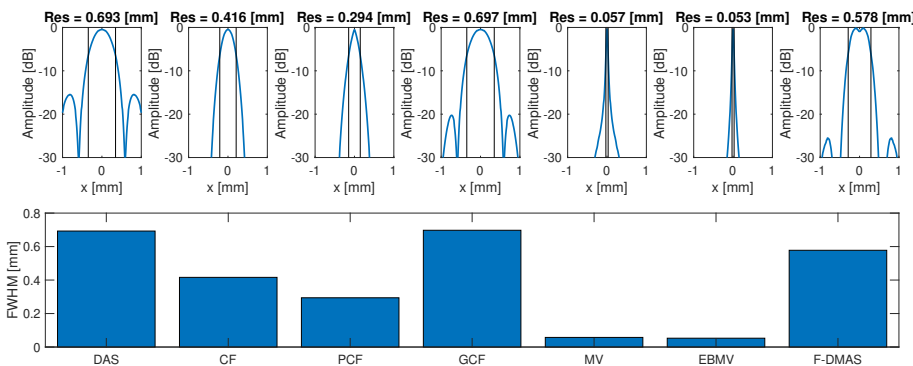


Figure 1.37: Full Width Half Maximum (FWHM) measured from a single point scatterer imaged by a plane wave transmission and reconstructed using the DAS, CF, PCF, GCF, MV, EBMV and F-DMAS beamformer.

Smaller FWHM means improved resolution if we define resolution to be an improved (narrower) reconstruction of the small point scatterer imaged. Judging by the results in Figure 1.37, all the adaptive beamformers tested, except GCF, have improved resolution compared to DAS.

1. Scientific Background: Software Beamforming Methodology

1.11.4 Resolution as separability

Improved resolution should result in improved separation of closely located targets. Let us now, instead of using the FWHM as a measure of resolution, define resolution to be the ability to resolve two scatterers. In Figure 1.38, we show in (a) the resulting images using the adaptive beamformers imaging two point scatterers separated by 1 mm. The plot below the B-mode images is the lateral line through the center of the points. The red dashed line is indicating -6 dB. When the scatterers are separated by 1 mm, all the beamformers expect GCF are able to detect both. Where detection is defined as a local minimum between the peaks of more than -6 dB.

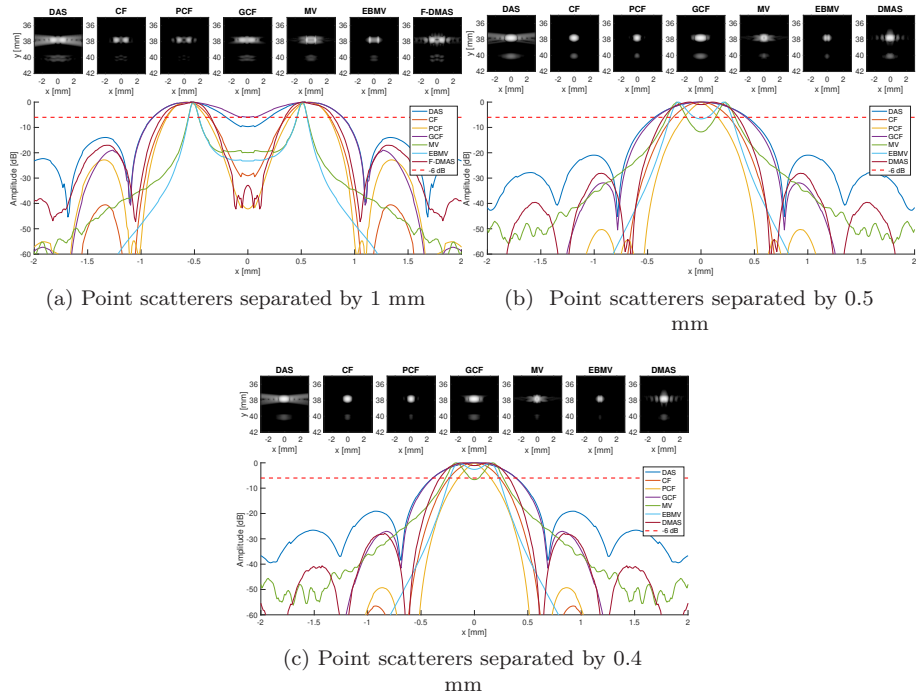


Figure 1.38: Images of two point scatterers separated by 1, 0.5 and 0.4 mm in (a), (b) and (c) respectively. The plot below the B-mode images are the lateral line through the center of the points. The red dashed line is indicating -6dB.

In Figure 1.38b only 0.5 mm is separating the point scatterers. Notice then that only the MV and EBMV are able to separate the two point scatterers. At 0.4 mm separation, in Figure 1.38c only the MV beamformer is able to separate the two points. When doing this study on more images with separation between the two point scatterers at 4, 2, 1, 0.5, 0.44 and 0.4 mm, we get the results in Figure 1.39. In the top graph, we see the separability, measured as the lowest point between the point scatterers for all beamformers with the dashed red line indicating the -6 dB limit.

In the bottom plot, we have, based on the -6 dB limit, divided the result from the beamformers into separated or not separated for all distances. Interestingly, only the MV and EBMV beamformer have better separability than DAS.

1.11. Evaluation of image quality – metrics

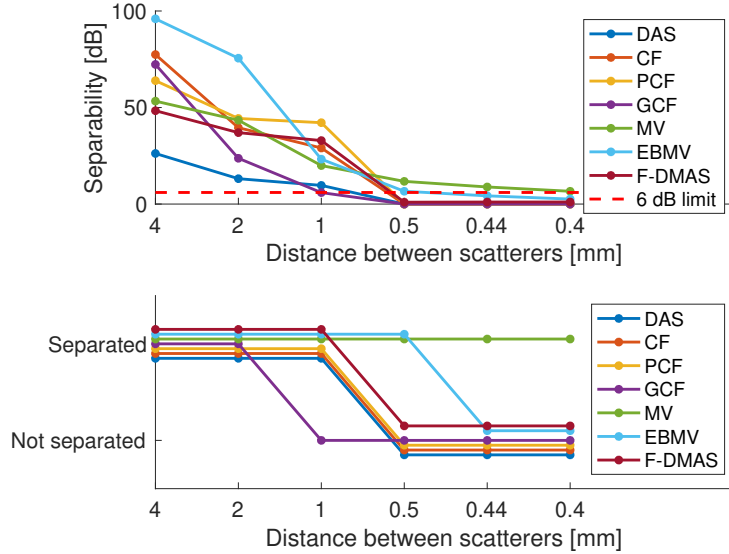


Figure 1.39: The measured separability, measured as the lowest point between the point scatterers, of two point scatterers separated by 4, 2, 1, 0.5, 0.44 and 0.4 mm in (a). The dashed red line indicate the 6dB separation. In (b) we have thresholded on the 6 dB limit, into separated or not separated.

Even though when we used the FWHM as the definition of resolution, all beamformers except GCF improved the FWHM compared to DAS. This short investigation shows some interesting results regarding the claimed improved resolution resulting from some adaptive beamformers. If the improved resolution, as measured by the FWHM does not result in improved separability, it is relevant to review the relevance of FWHM as a metric for resolution. Also, if we tie our preliminary results on resolution improvement with our previous categorization of the adaptive beamformers we can hypothesize an interesting connection. The beamformers categorized to the *image weight* category, according to categorization II in Section 1.8.8, have an improved FWHM. But they do not have an improved separability compared to DAS. This makes, of course, sense since the adaptive beamformers belonging to the *image weight* category is taking the DAS image and multiplying it with an adaptive weight. This will, of course, result in narrower FWHM, in the same way as simply raising the DAS image to a power > 1 . However, simply raising the image to a power does not yield new information. Interestingly, this did not apply to the GCF in our tested scenario. Whether multiplying an image with an adaptive weight yields improved information in terms of resolutions remains to be investigated in depth. But our brief investigation here shows that one can question the ability to resolve scatterers. Thus, we have identified that as with contrast, there seems to be no consensus on how to measure resolution in medical ultrasound imaging. Similar to the thorough investigation into contrast and contrast metrics of adaptive beamformers, as we have done in the published papers, needs to be done for resolution. However, such an investigation into resolution is not done in this thesis and remains to be further studied.

Appendices

APPENDIX A

The Hilbert Transform

The Hilbert transform is used excessively through this thesis, and therefore deserves a closer description. The Hilbert transform is an operation that shifts the phase of a signal $x(t)$ by $-\frac{\pi}{2}$. In time domain the phase shifted signal $\hat{x}(t)$ is given by the convolution

$$\hat{x}(t) = \frac{1}{\pi t} * x(t). \quad (\text{A.1})$$

In frequency domain the Hilbert transform acts as a filter with transfer function

$$H(f) = \begin{cases} -i = e^{+\frac{i\pi}{2}} & , f > 0 \\ 0 & , f = 0 \\ i = e^{-\frac{i\pi}{2}} & , f < 0 \end{cases} \quad (\text{A.2})$$

And this is where the interesting stuff happens. This means that the negative frequencies will be shifted by a phase of $-\frac{\pi}{2}$ and the positive frequencies with $+\frac{\pi}{2}$.

In this thesis we are using the Hilbert transform for two reasons. To create the analytic signal, and to find the envelope of a signal.

A.1 Analytic signal

The analytic signal

$$x_a[n] = x[n] + j(\hat{x}[n]) \quad | \quad \hat{x}[n]: \text{Hilbert transform of } x[n]. \quad (\text{A.3})$$

is the one-sided representation of a real-valued signal. The idea is that the negative frequency components in the Fourier spectrum of a real-valued signal is redundant and can be discarded without any loss of information. This gives us a complex signal, which in many cases is beneficial as it facilitates many signal processing techniques. For example it allows us to use complex weights for Capon's Minimum Variance beamformer 1.8.1 allowing a non-symmetric beampattern. As long as the signal processing techniques does not introduce negative frequencies we can convert back to a real signal by just discarding the imaginary part.

In Figure A.1 we demonstrate what we just discussed.

A. The Hilbert Transform

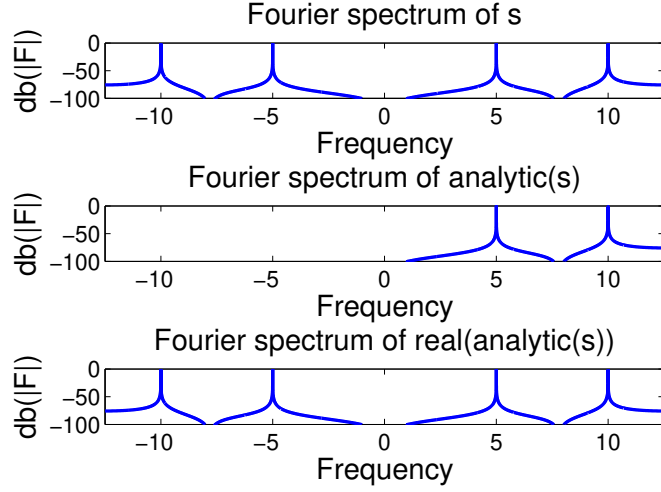


Figure A.1: The top is the Fourier spectrum of a signal consisting of two sinusoids with frequency 5 and 10. The signal is real so the first spectrum is two-sided. The middle plot is the spectrum of the analytic signal as defined above, and the bottom plot is the Fourier spectrum of just the real part of the analytic signal. We see that as expected no information is lost in the signal.

A.2 Envelope of signal

The envelope of the signal can easily be found by taking the magnitude of the analytic signal $A[n] = |x_a[n]| = \sqrt{x[n]^2 + \hat{x}[n]^2}$ this follows from the fact that the Hilbert transform is a $\frac{\pi}{2}$ phase shift of the signal, see Figure A.2 where *signal* is $x[n]$ and *Hilbert(s)* is $\hat{x}[n]$, so the square root of the sum of squares of the two signals will intuitively be the envelope.

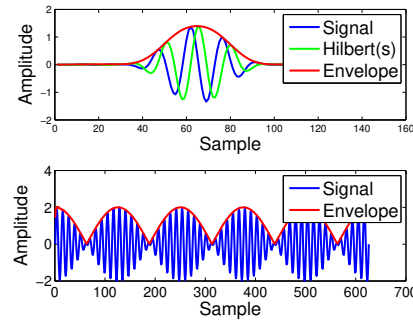


Figure A.2: The top is displaying the signal, the Hilbert transform of the signal and the envelope of the signal. The bottom shows the signal and the envelope of the signal.

APPENDIX B

Deriving the two-way resolution

The one way angular resolution at -6dB can be approximated by (Harris, 1978)

$$\theta_{6dB} \approx \frac{1.21\lambda}{D}, \quad (\text{B.1})$$

where D is the size of the full array aperture and λ is the wavelength.

We will now derive an expression for the two-way resolution. Assuming point sources and that the same sized array is used on both transmit (tx) and receive (rx). We know that the two-way beampattern can be calculated by taking the square of the one way beampattern (Johnson and Dugdeon, 1993)

$$W_{\text{two way}} = W_{tx} W_{rx} = W_{\text{one way}}^2. \quad (\text{B.2})$$

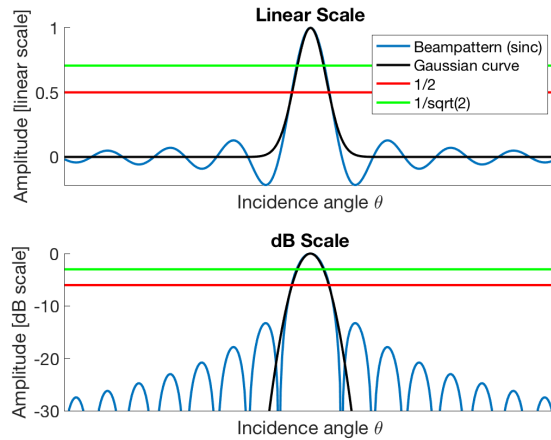


Figure B.1: The beampattern, a *sinc*, for some array with size D for some wavelength λ together with a Gaussian with zero mean and some standard variation σ . In the top we have plotted the beampattern and the Gaussian in linear scale, while we in the bottom have plotted them in dB scale. We have also indicated $1/2$ and $1/\sqrt{2}$ in the linear scale, resulting at $\approx -6\text{dB}$ and $\approx -3\text{dB}$ in the dB scale.

From Figure B.1, we see that the central part of the mainlobe of the beampattern can be approximated by a Gaussian curve. In Figure B.1 we have

B. Deriving the two-way resolution

plotted the beampattern, a *sinc*, for some array with size D for some wavelength λ together with a normalized Gaussian with zero mean and some standard variation σ . In the top of Figure B.1 we have plotted the beampattern and the Gaussian curve in linear scale, while we in the bottom have plotted them in dB scale. We have also indicated $1/2$ and $1/\sqrt{2}$ in the linear scale, resulting at $\approx -6\text{dB}$ and $\approx -3\text{dB}$ in the dB scale.

Using a normalized Gaussian curve we can find the half width, h , of the mainlobe at $\frac{1}{2}$ in linear scale (corresponding to -6dB) by

$$\begin{aligned} \frac{1}{2} &= e^{\frac{-h^2}{2\sigma^2}} \\ \ln\left(\frac{1}{2}\right) &= \frac{-h^2}{2\sigma^2} \\ \Downarrow \\ h^2 &= -2 \ln\left(\frac{1}{2}\right) \sigma^2 = 2 \ln(2) \sigma^2. \end{aligned}$$

While at the $\frac{1}{\sqrt{2}}$ (corresponding to -3dB) we find the half width, g , of the mainlobe by

$$\frac{1}{\sqrt{2}} = e^{\frac{-g^2}{2\sigma^2}} \quad (\text{B.3})$$

$$\ln\left(\frac{1}{\sqrt{2}}\right) = \frac{-g^2}{2\sigma^2} \quad (\text{B.4})$$

$$\Downarrow \quad (\text{B.5})$$

$$g^2 = -2 \ln\left(\frac{1}{\sqrt{2}}\right) \sigma^2 = \ln(2) \sigma^2. \quad (\text{B.6})$$

The g and h is only half the width of the mainlobe, and thus to get the full width we need to multiply with 2. The relationship between the $\theta_{-3\text{dB}}$ and $\theta_{-6\text{dB}}$, but in linear scale, is then

$$\frac{2g}{2h} = \frac{2\sqrt{\ln(2)\sigma^2}}{2\sqrt{2\ln(2)\sigma^2}} = \frac{1}{\sqrt{2}}. \quad (\text{B.7})$$

Finally, using that $W_{\text{two way}} = W_{\text{one way}}^2$, then $W_{\text{two way } 6\text{dB}} = W_{\text{one way } 3\text{dB}}$ as illustrated in Figure B.2.

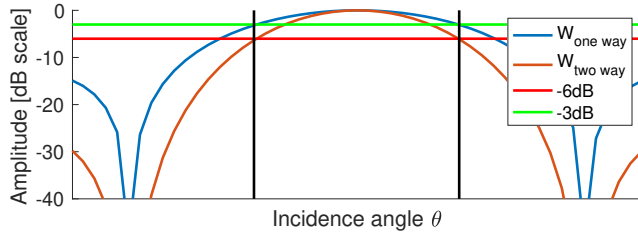


Figure B.2: The one-way and two-way beampattern plotted indicating that $W_{\text{two way } 6dB} = W_{\text{one way } 3dB}$.

We get

$$\theta_{6dB \text{ two way}} = \frac{1}{\sqrt{2}} \theta_{3dB \text{ one way}} = \frac{1}{\sqrt{2}} \frac{1.21\lambda}{D}, \quad (\text{B.8})$$

and if we use a small angle approximation at depth z

$$x_{\text{res two way}} = \frac{1}{\sqrt{2}} x_{\text{res one way}} = \frac{1.21\lambda z}{\sqrt{2}D}. \quad (\text{B.9})$$

Bibliography

- Applebaum, S. (Sept. 1976). ‘Adaptive arrays’. In: *IEEE Transactions on Antennas and Propagation* 24.5, pp. 585–598. doi: [10.1109/TAP.1976.1141417](https://doi.org/10.1109/TAP.1976.1141417).
- Asl, B. M. and Mahloojifar, A. (2010). ‘Eigenspace-based minimum variance beamforming applied to medical ultrasound imaging’. In: *IEEE Transactions on Ultrasonics, Ferroelectrics, and Frequency Control* 57.11, pp. 2381–2390. doi: [10.1109/TUFFC.2010.1706](https://doi.org/10.1109/TUFFC.2010.1706).
- Bae, M. H. (2000). ‘A study of synthetic-aperture imaging with virtual source elements in B-mode ultrasound imaging systems’. In: *IEEE Transactions on Ultrasonics, Ferroelectrics, and Frequency Control* 47.6, pp. 1510–1519. doi: [10.1109/58.883540](https://doi.org/10.1109/58.883540).
- Boni, E., Yu, A. C., Freear, S., Jensen, J. A. and Tortoli, P. (2018). ‘Ultrasound open platforms for next-generation imaging technique development’. In: *IEEE Transactions on Ultrasonics, Ferroelectrics, and Frequency Control* 65.7, pp. 1078–1092. doi: [10.1109/TUFFC.2018.2844560](https://doi.org/10.1109/TUFFC.2018.2844560).
- Bryn, F. (1962). ‘Optimum Signal Processing of Three-Dimensional Arrays Operating on Gaussian Signals and Noise’. In: *The Journal of the Acoustical Society of America* 34.3, pp. 289–297. doi: [10.1121/1.1928112](https://doi.org/10.1121/1.1928112).
- Camacho, J., Parrilla, M. and Fritsch, C. (2009). ‘Phase coherence imaging’. In: *IEEE Transactions on Ultrasonics, Ferroelectrics, and Frequency Control* 56.5, pp. 958–974. doi: [10.1109/TUFFC.2009.1128](https://doi.org/10.1109/TUFFC.2009.1128).
- Capon, J. (Apr. 1964). ‘Optimum weighting functions for the detection of sampled signals in noise’. In: *IEEE Transactions on Information Theory* 10.2, pp. 152–159. doi: [10.1109/TIT.1964.1053664](https://doi.org/10.1109/TIT.1964.1053664).
- Chau, G., Lavarello, R. and Dahl, J. (2016). ‘Short-Lag Spatial Coherence Weighted Minimum Variance Beamformer for Plane-wave Images’. In: pp. 1–3.
- Denarie, B., Tangen, T. A., Ekroll, I. K., Rolim, N., Torp, H. and Lovstakken, L. (2013). ‘Coherent Plane Wave Compounding for Very High Frame Rate Ultrasonography of Rapidly Moving Targets’. In: 32.7, pp. 1265–1276.
- Diamantis, K., Anderson, T., Butler, M. B., Villagomez-Hoyos, C. A., Jensen, J. A. and Sboros, V. (2019). ‘Resolving ultrasound contrast microbubbles using minimum variance beamforming’. In: *IEEE Transactions on Medical Imaging* 38.1, pp. 194–204. doi: [10.1109/TMI.2018.2859262](https://doi.org/10.1109/TMI.2018.2859262).
- Flax, S. W. and O’Donnell, M. (Nov. 1988). ‘Phase-aberration correction using signals from point reflectors and diffuse scatterers: basic principles’. In:

Bibliography

- IEEE Transactions on Ultrasonics, Ferroelectrics, and Frequency Control* 35.6, pp. 758–767. DOI: 10.1109/58.9333.
- Franceschetti, G. and Lanari, R. (1999). *Synthetic Aperture Radar Processing*. Electronic Engineering Systems. Taylor & Francis.
- Frazier, C. H. and O'Brien, W. D. (1998). ‘Synthetic aperture techniques with a virtual source element’. In: *IEEE Transactions on Ultrasonics, Ferroelectrics, and Frequency Control* 45.1, pp. 196–207. DOI: 10.1109/58.646925.
- Freeman, S., Li, P. C. and Odonnell, M. (1995). ‘Retrospective Dynamic Transmit Focusing’. In: *Ultrasonic Imaging* 17.3, pp. 173–196. DOI: <https://doi.org/10.1006/uimg.1995.1008>.
- Harris, F. J. (1978). ‘On the Use of Windows for Harmonic Analysis with the Discrete Fourier Transform’. In: *Proceedings of the IEEE* 66.1, pp. 51–83.
- Hergum, T., Bjåstad, T., Kristoffersen, K. and Torp, H. (2007). ‘Parallel beamforming using synthetic transmit beams’. In: *IEEE Transactions on Ultrasonics, Ferroelectrics and Frequency Control* 54.2.
- Holm, S. (2019). *Waves with Power-Law Attenuation*. Vol. 1. Norway: Springer International Publishing. DOI: 10.1007/978-3-030-14927-7.
- Hverven, S., Rindal, O. M. H., Rodriguez-Molarez, A. and Austeng, A. (2017). ‘The Influence of Speckle Statistics on Contrast Metrics in Ultrasound Imaging’. In: *IEEE International Ultrasonics Symposium*. DOI: 10.1109/ULTSYM.2017.8091875.
- Jensen, A. and Austeng, A. (2014). ‘The iterative adaptive approach in medical ultrasound imaging’. In: *IEEE Transactions on Ultrasonics, Ferroelectrics, and Frequency Control* 61.10, pp. 1688–1697. DOI: 10.1109/TUFFC.2014.006478.
- Jensen, J. A. (1996). ‘Field: A program for simulating ultrasound systems’. In: *Medical & Biological Engineering & Computing* 34, pp. 351–353.
- Jensen, J. A., Nikolov, S. I., Gammelmark, K. L. and Peders, M. H. (2006). ‘Synthetic aperture ultrasound imaging’. In: *Ultrasonics* 44. DOI: 10.1016/j.ultras.2006.07.017.
- Jensen, J. A. and Svendsen, N. B. (1992). ‘Calculation of Pressure Fields from Arbitrarily Shaped, Apodized, and Excited Ultrasound Transducers’. In: *IEEE Transactions on Ultrasonics, Ferroelectrics and Frequency Control* 39.2, pp. 262–267.
- Johnson, D. H. and Dudgeon, D. E. (1993). *Array Signal Processing: Concepts and Techniques*. Prentice-Hall signal processing series. P.T.R. Prentice-Hall.
- Johnson, D. H. and Dugdeon, D. E. (1993). *Array signal processing: Concepts and techniques*. Vol. Prentice-Hall signal processing series. UpperSaddle River, NJ 07458: P.T.R. Prentice-Hall.
- Kaczkowski, P. (2016). ‘Bandwidth Sampling Data Acquisition with the Vantage System for High Frequency Transducers’. In: *Verasonics Inc. White Paper*.
- Krishnan, S., Rigby, K. W. and O’Donnell, M. (1997). ‘Improved estimation of phase aberration profiles’. In: *IEEE Transactions on Ultrasonics, Ferroelectrics, and Frequency Control* 44.3, pp. 701–713. DOI: 10.1109/58.658333.
- Kulina, R., Agarwal, S., Wiley, B., Narula, J., Sengupta, P. P. and Chaudhry, F. A. (2016). ‘New Software Beamforming Algorithm is Superior to Standard Hardware-Based Beamformer in Endocardial Border Detection’. In: *GE Healthcare Whitepaper, GE Symposium 2016*, pp. 1–4.

Bibliography

- Lediju, M. A., Trahey, G. E., Byram, B. C. and Dahl, J. J. (2011). ‘Short-lag spatial coherence of backscattered echoes: Imaging characteristics’. In: *IEEE Transactions on Ultrasonics, Ferroelectrics, and Frequency Control* 58.7, pp. 1377–1388. DOI: [10.1109/TUFFC.2011.1957](https://doi.org/10.1109/TUFFC.2011.1957).
- Lediju Bell, M. A., Goswami, R., Kisslo, J. A., Dahl, J. J. and Trahey, G. E. (2013). ‘Short-Lag Spatial Coherence (SLSC) Imaging of Cardiac Ultrasound Data: Initial Clinical Results’. In: *Ultrasound in medicine & biology* 39.10, pp. 1861–1874. DOI: [10.1016/j.ultrasmedbio.2013.03.029](https://doi.org/10.1016/j.ultrasmedbio.2013.03.029).
- Li, P. C. and Li, M. L. (2003). ‘Adaptive imaging using the generalized coherence factor’. In: *IEEE Transactions on Ultrasonics, Ferroelectrics, and Frequency Control* 50.2, pp. 128–141. DOI: [10.1109/TUFFC.2003.1182117](https://doi.org/10.1109/TUFFC.2003.1182117).
- Liebgott, H., Rodriguez-Molares, A., Cervenansky, F., Jensen, J. A. and Bernard, O. (2016). ‘Plane-Wave Imaging Challenge in Medical Ultrasound’. In: *IEEE International Ultrasonics Symposium, IUS* 2016-Novem. DOI: [10.1109/ULTSYM.2016.7728908](https://doi.org/10.1109/ULTSYM.2016.7728908).
- Mallart, R. and Fink, M. (1991). ‘The van Cittert-Zernike theorem in pulse echo measurements’. In: *Journal of Acoustical Society of America* 90.November 1991, pp. 2718–2727.
- (1994). ‘Adaptive focusing in scattering media through sound-speed inhomogeneities: The van Cittert Zernike approach and focusing criterion’. In: *The Journal of the Acoustical Society of America* 96.6, p. 3721. DOI: [10.1121/1.410562](https://doi.org/10.1121/1.410562).
- Mann, J. A. and Walker, W. F. (Oct. 2002). ‘A constrained adaptive beamformer for medical ultrasound: initial results’. In: *2002 IEEE Ultrasonics Symposium, 2002. Proceedings*. Vol. 2, 1807–1810 vol.2. DOI: [10.1109/ULTSYM.2002.1192650](https://doi.org/10.1109/ULTSYM.2002.1192650).
- Matrone, G., Savoia, A. S. and Magenes, G. (2015). ‘The Delay Multiply and Sum Beamforming Algorithm in Ultrasound B-Mode Medical Imaging’. In: *IEEE Transactions on Medical Imaging* 34.4, pp. 940–949.
- McNeil Jr., D. G. (15th Apr. 2019). *In African Villages, These Phones Become Ultrasound Scanners*. URL: <https://www.nytimes.com/2019/04/15/health/medical-scans-butterfly-iq.html> (visited on 06/06/2019).
- Mehdizadeh, S., Austeng, A., Johansen, T. F. and Holm, S. (2012). ‘Eigenspace based minimum variance beamforming applied to ultrasound imaging of acoustically hard tissues’. In: *IEEE Transactions on Medical Imaging* 31.10, pp. 1912–1921. DOI: [10.1109/TMI.2012.2208469](https://doi.org/10.1109/TMI.2012.2208469).
- Montaldo, G., Tanter, M., Bercoff, J., Benech, N. and Fink, M. (2009). ‘Coherent plane-wave compounding for very high frame rate ultrasonography and transient elastography’. In: *IEEE Transactions on Ultrasonics, Ferroelectrics, and Frequency Control* 56.3, pp. 489–506. DOI: [10.1109/TUFFC.2009.1067](https://doi.org/10.1109/TUFFC.2009.1067).
- Nguyen, N. Q. and Prager, R. W. (2018). ‘A Spatial Coherence Approach to Minimum Variance Beamforming for Plane-Wave Compounding’. In: *IEEE Transactions on Ultrasonics, Ferroelectrics, and Frequency Control* PP.99, pp. 1–1. DOI: [10.1109/TUFFC.2018.2793580](https://doi.org/10.1109/TUFFC.2018.2793580).
- Nguyen, N. Q. and Prager, R. W. (2016). ‘High-Resolution Ultrasound Imaging With Unified Pixel-Based Beamforming’. In: *IEEE Trans. Med. Imaging* 35.1, pp. 98–108.
- Nikolov, S. I., Kortbek, J. and Jensen, J. A. (2010). ‘Practical applications of synthetic aperture imaging’. In: *2010 IEEE International Ultrasonics Symposium*, pp. 350–358. DOI: [10.1109/ULTSYM.2010.5935627](https://doi.org/10.1109/ULTSYM.2010.5935627).

Bibliography

- Nock, L., Trahey, G. E. and Smith, S. W. (1989). ‘Phase aberration correction in medical ultrasound using speckle brightness as a quality factor’. In: *The Journal of the Acoustical Society of America* 85.5, pp. 1819–1833.
- Ozkan, E., Vishnevsky, V. and Goksel, O. (2018). ‘Inverse Problem of Ultrasound Beamforming with Sparsity Constraints and Regularization’. In: *IEEE Transactions on Ultrasonics, Ferroelectrics, and Frequency Control* PP.99, pp. 1–1. doi: [10.1109/TUFFC.2017.2757880](https://doi.org/10.1109/TUFFC.2017.2757880).
- Palmer, C. L., Rindal, O. M. H., Holm, S. and Austeng, A. (2016). ‘Realtime plane-wave software beamforming with an iPhone’. In: *IEEE International Ultrasonics Symposium, IUS*, pp. 1–4. doi: [10.1109/ULTSYM.2016.7728408](https://doi.org/10.1109/ULTSYM.2016.7728408).
- Papadacci, C., Pernot, M., Couade, M., Fink, M. and Tanter, M. (2014). ‘High-contrast ultrafast imaging of the heart’. In: *IEEE Transactions on Ultrasonics, Ferroelectrics, and Frequency Control* 61.2, pp. 288–301. doi: [10.1109/TUFFC.2014.6722614](https://doi.org/10.1109/TUFFC.2014.6722614).
- Patterson, M. and Foster, F. (1983). ‘The Improvement and quantitative assessment of b-mode images produced by an annular array/cone hybrid’. In: *Ultrasonic Imaging* 5, pp. 195–213.
- Prieur, F., Rindal, O. M. H. and Austeng, A. (2018). ‘Signal Coherence and Image Amplitude With the Filtered Delay Multiply and Sum Beamformer’. In: *IEEE Transactions on Ultrasonics, Ferroelectrics, and Frequency Control*. doi: [10.1109/TUFFC.2018.2831789](https://doi.org/10.1109/TUFFC.2018.2831789).
- Proakis, J. and Manolakis, D. (2007). *Digital Signal Processing*. Pearson Prentice Hall.
- Rayleigh, L. J. W. S. (1879). ‘Investigations in optics, with special reference to the spectroscope’. In: *The London, Edinburgh, and Dublin Philosophical Magazine and Journal of Science* 8.49, pp. 261–274. doi: [10.1080/14786447908639684](https://doi.org/10.1080/14786447908639684).
- Rindal, O. M. H., Aakhus, S., Holm, S. and Austeng, A. (2017). ‘Hypothesis of Improved Visualization of Microstruc in the Interventricular Septum with Ultrasound and Adaptive Beamforming’. In: *Ultrasound in Medicine and Biology*. doi: [10.1016/j.ultrasmedbio.2017.05.023](https://doi.org/10.1016/j.ultrasmedbio.2017.05.023).
- Rindal, O. M. H. and Austeng, A. (2016). ‘Double Plane-Wave Imaging’. In: *IEEE International Ultrasonics Symposium*. doi: [10.1109/ULTSYM.2016.7728906](https://doi.org/10.1109/ULTSYM.2016.7728906).
- Rindal, O. M. H., Austeng, A., A., F. and Rodriguez-Molarez, A. (2019). ‘The Effect of Dynamic Range Alterations in the Estimation of Contrast’. In: *IEEE Transactions on Ultrasonics, Ferroelectrics, and Frequency Control*. doi: [10.1109/TUFFC.2019.2911267](https://doi.org/10.1109/TUFFC.2019.2911267).
- Rindal, O. M. H., Rodriguez-Molares, A. and Austeng, A. (2018). ‘A simple, artifact-free, virtual source model’. In: *IEEE International Ultrasonics Symposium*. doi: [10.1109/ULTSYM.2018.8579944](https://doi.org/10.1109/ULTSYM.2018.8579944).
- Rindal, O. M. H., Rodriguez-Molarez, A. and Austeng, A. (2017). ‘The Dark Region Artifact in Adaptive Ultrasound Beamforming’. In: *IEEE International Ultrasonics Symposium*. doi: [10.1109/ULTSYM.2017.8092255](https://doi.org/10.1109/ULTSYM.2017.8092255).
- Rindal, O. M. H. (2018). *Achieving uniform field of view (FOV) in synthetic aperture imaging (STAI) in Field II simulations*. URL: <http://www.ustb.no/examples/uniform-fov-in-field-ii-simulations/> (visited on 05/06/2018).
- Rodriguez-Molares, A., Rindal, O. M. H., Bernard, O., Nair, A., Lediju Bell, M., Liebgott, H., Austeng, A. and Løvstakken, L. (2017). ‘The Ultrasound

Bibliography

- ToolBox'. In: *IEEE International Ultrasonics Symposium*. DOI: [10.1109/ULTSYM.2017.8092389](https://doi.org/10.1109/ULTSYM.2017.8092389).
- Rodriguez-Molares, A., Torp, H., Denarie, B. and Løvstakken, L. (2015). 'The Angular Apodization in Coherent Plane-Wave Compounding'. In: *IEEE transactions on ultrasonics, ferroelectrics, and frequency control* 62.11, pp. 2018–2023.
- Rodriguez-Molarez, A., Rindal, O. M. H., D'hooge, J., Måsøy, S.-E., Austeng, A., Lediju Bell, M. and Torp, H. (2019). 'The Generalized Contrast-to-Noise ratio'. In: *IEEE Transactions on Ultrasonics, Ferroelectrics, and Frequency Control*.
- Sasso, M. and Cohen-Bacrie, C. (2005). 'Medical Ultrasound Using The Fully Adaptive Beamformer'. In: *IEEE International Conference on Acoustical Speech and Signal Processing, 2015. Proceedings (ICAASP 05)*. 2.4, pp. 489–492.
- Shattuck, D. P., Weinshenker, M. D., Smith, S. W. and Ramm, O. T. von (1984). 'Explososcan: A parallel processing technique for high speed ultrasound imaging with linear phased arrays'. In: *The Journal of the Acoustical Society of America* 75.4, pp. 1273–1282. DOI: [10.1121/1.390734](https://doi.org/10.1121/1.390734).
- Shin, J. and Huang, L. (2017). 'Spatial Prediction Filtering of Acoustic Clutter and Random Noise in Medical Ultrasound Imaging'. In: *IEEE Transactions on Medical Imaging* 36.2, pp. 396–406. DOI: [10.1109/TMI.2016.2610758](https://doi.org/10.1109/TMI.2016.2610758).
- Siemens Healthineers (2019). *A Honeymoon at Siemens - The story of the first ultrasound image of a beating heart*. URL: <https://www.medmuseum.siemens-healthineers.com/en/stories-from-the-museum/echokardiographie> (visited on 06/05/2019).
- Smith, S., Lopez, H. and Bodine, W. (1985). 'Frequency independent ultrasound contrast-detail analysis'. In: *Ultrasound in Medicine & Biology* 11.3, pp. 467–477. DOI: [https://doi.org/10.1016/0301-5629\(85\)90158-9](https://doi.org/10.1016/0301-5629(85)90158-9).
- Soni, N. J., Arntfield, R. and Kory, P. (2014). *Point of Care Ultrasound E-book*. Elsevier Health Sciences.
- Steinberg, B. D. (1976). *Principles of Aperture and Array System Design*. John Wiley & Sons.
- SuperSonic Imagine (2019). *Aixplorer*. URL: <https://www.supersonicimagine.com> (visited on 06/05/2019).
- Synnevåg, J., Austeng, A. and Holm, S. (Sept. 2005). 'Minimum variance adaptive beamforming applied to medical ultrasound imaging'. In: *IEEE Ultrasonics Symposium, 2005*. Vol. 2, pp. 1199–1202. DOI: [10.1109/ULTSYM.2005.1603066](https://doi.org/10.1109/ULTSYM.2005.1603066).
- Synnevåg, J.-F., Austeng, A. and Holm, S. (2009). 'Benefits of minimum-variance beamforming in medical ultrasound imaging'. In: *Ultrasonics, Ferroelectrics and Frequency Control, IEEE Transactions on* 56.9, pp. 1868–1879.
- Szabo, T. L. (2013). *Diagnostic Ultrasound Imaging: Inside Out*. Second Edi. Biomedical Engineering. Elsevier Science.
- Szasz, T., Basarab, A. and Kouamé, D. (2016). 'Strong reflector-based beamforming in ultrasound medical imaging'. In: *Ultrasonics* 66, pp. 111–124. DOI: [10.1016/j.ultras.2015.11.003](https://doi.org/10.1016/j.ultras.2015.11.003). arXiv: [1507.08184](https://arxiv.org/abs/1507.08184).
- Viola, F. and Walker, W. (2005). 'Adaptive signal processing in medical ultrasound beamforming'. In: *Proceedings IEEE Ultrasonics Symposium* 4.c, pp. 1980–1983. DOI: [10.1109/ULTSYM.2005.1603264](https://doi.org/10.1109/ULTSYM.2005.1603264).

Bibliography

- Von Ramm, O. T. and Thurstone, F. L. (1975). ‘Thaumascan: design considerations and performance characteristics’. In: *Ultrasound in medicine*. Springer, pp. 373–378.
- Wagner, R. F., Smith, S. W., Sandrik, J. M. and Lopez, H. (1983). ‘Statistics of Speckle in Ultrasound B-Scans’. In: *IEEE Transactions on Sonics and Ultrasonics* 30.3.
- Wang, Z., Li, J. and Wu, R. (2005). ‘Time-delay- And time-reversal-based robust Capon beamformers for ultrasound imaging’. In: *IEEE Transactions on Medical Imaging* 24.10, pp. 1308–1322. DOI: [10.1109/TMI.2005.857222](https://doi.org/10.1109/TMI.2005.857222).
- Whittingham, T. A. (2007). ‘Medical diagnostic applications and sources’. In: *Progress in Biophysics and Molecular Biology* 93.
- Widrow, B., Mantey, P. E., Griffiths, L. J. and Goode, B. B. (1967). ‘Adaptive antenna systems’. In: *Proceedings of the IEEE* 55.12, pp. 2143–2159. DOI: [10.1109/PROC.1967.6092](https://doi.org/10.1109/PROC.1967.6092).
- Wright, J. N. (1997). ‘Image Formation in Diagnostic Ultrasound’. In: *IEEE International Ultrasonics Symposium*.
- Zhao, J., Wang, Y., Yu, J., Guo, W., Zhang, S. and Aliabadi, S. (2017). ‘Short-lag Spatial Coherence Ultrasound Imaging with Adaptive Synthetic Transmit Aperture Focusing’. In: *Ultrasonic Imaging* 39.4. PMID: 28068874, pp. 224–239. DOI: [10.1177/0161734616688328](https://doi.org/10.1177/0161734616688328).
- Zhuang, B., Rohling, R. and Abolmaesumi, P. (2018). ‘Accumulated Angle Factor-Based Beamforming to Improve the Visualization of Spinal Structures in Ultrasound Images’. In: *IEEE Transactions on Ultrasonics, Ferroelectrics, and Frequency Control* 65.2, pp. 210–222. DOI: [10.1109/TUFFC.2017.2781726](https://doi.org/10.1109/TUFFC.2017.2781726).